Marine and Petroleum Geology 163 (2024) 106776

Contents lists available at ScienceDirect

Marine and Petroleum Geology

journal homepage: www.elsevier.com/locate/marpetgeo

Fluid tracing and evolution at micron-scale of shales in faulted lake basin: Evidence and constraints from in-situ analysis of analcime

Junran Wang [a,b], Chao Liang [a,b,c,*], Yingchang Cao [a,b,c], Shunyao Song [f], Keyu Liu [a,b], Shengyu Yang [a,b], Jinqiang Tian [a,b], Danish Khan [d,e], Bixiao Xin [g]

[a] National Key Laboratory of Deep Oil and Gas, China University of Petroleum (East China), Qingdao, 266580, China
[b] School of Geosciences, China University of Petroleum, Qingdao, 266000, China
[c] Laboratory for Marine Mineral Resource, Qingdao National Laboratory for Marine Science and Technology, Qingdao, 266071, China
[d] State Key Laboratory of Ore Deposit Geochemistry, Institute of Geochemistry, Chinese Academy of Sciences, Guiyang, 550002, China
[e] University of Chinese Academy of Sciences, Beijing, 100049, China
[f] PetroChina Dagang Oil Field Company, Tianjin, 300280, China
[g] Center of Deep Sea Research, Institute of Oceanology, Chinese Academy of Sciences, Qingdao, 266071, China

ARTICLE INFO

Keywords:
Fluid tracing and evolution
Analcime
Faulted lake basin
Lacustrine shales
Bohai bay basin

ABSTRACT

The Huanghua Depression in the Bohai Bay Basin has experienced significant development of massive NNE-NE faults, influenced by the Eocene activation of the Lanliao Fault and its subsequent Oligocene dextral intensification. These faults serve as a conduit for connate fluid and magmatic hydrothermal fluid (MHF), thereby forming a complex fluid system. Gaining an understanding of these fluid activities is essential for research into mass balance and hydrocarbon migration within shales. This study explores the origin and distribution of analcime, aligns the fluid evolution stage with different analcime types, and constructs a comprehensive water-rock reaction sequence. The study identifies six types of analcime based on occurrence characteristics (occurring as laminae, lens, fracture filling, bioshell filling, vein marginal crystal and cement). The above six types of analcime is further classified into hydrothermal fluid origin analcime (HFOA: include analcime cement, vein marginal crystal, lens, fracture filling and bioshell filling) and connate fluid origin analcime (CFOA: analcime laminae) based on major elemental indicators (Si/Al and 10K/(10K + Na)). HFOA has lower ∑REE (rare earth element) and strong positive correlation between ∑REE and LILEs (large ionic lithophilic elements); while CFOA has higher ∑REE and weak positive correlation between ∑REE and LILEs. Different analcime types correlate with varying fluid properties and transport stages. HFOA forms during MHF upwelling. After the MHF entering and mixing with the lake water, thermal repulsions between the crystal particles made it move to form fine-grained sedimentary layer, the connate fluid trapped in pores directly precipitate to form CFOA, or form CFOA by modifying clay minerals and feldspars. Considering the tectonic context, we infer that the formation of analcime was primarily driven by high-frequency, low-intensity magmatism, governed by the activation of Lanliao deep fault. The study of analcime can aid in identifying and classifying fluid activity processes, offering a novel perspective for investigating sedimentation and diagenesis in continental shales.

1. Introduction

Fluid migration is now recognized as playing a major role in virtually all geologic processes (Cathles, 1990). Magmatic hydrothermal fluid (MHF), derived from mantle sources, serves as carrier for material and energy transfer. They significantly influence sedimentary and diagenetic evolution within basins (Fyfe, 1997; Liu et al., 2019). The duration and magnitude of MHF activities are coupled to the tectonic evolution of the crust, controlled by the development of regional basement fractures and shallow fracture systems (Oliver, 1986; Luo et al., 2017; Zhu et al., 2020; Tao et al., 2022; Cheng et al., 2022). MHF interacts with connate fluid and lake water along the fracture upwelling pathway, the mixing of shallow oxygenated groundwater with the basinal fluids results in variable fluid properties (Garven, 1995; Boles et al., 2004). This interaction results in the formation of mineral assemblages through complex water-rock interactions with the surrounding rock (Bennett et al., 2008;

* Corresponding author. National Key Laboratory of Deep Oil and Gas, China University of Petroleum (East China), Qingdao 266580, China.
E-mail address: liangchao0318@163.com (C. Liang).

https://doi.org/10.1016/j.marpetgeo.2024.106776
Received 27 December 2023; Received in revised form 23 February 2024; Accepted 28 February 2024
Available online 14 March 2024

Prol-Ledesma et al., 2010; Urubek et al., 2015; Han et al., 2021). Hydrothermal mineral elemental composition has different enrichment patterns at different stages of fluid evolution due to migration and crystallization mechanisms. This variability provides a foundation for the inversion of fluid evolution and tectonic activities (Barrat et al., 2000; Zhang, 2008; Himmler et al., 2013; Columbu, 2018; Zwicker et al., 2018). Hydrothermal systems are widely developed in the faulted basins of eastern China, driven by the activation of Cenozoic deep faults and mantle-derived magmatism (Ochoa et al., 2007; Sun et al., 2014; Su et al., 2011). At present, studies on the evolution of MHF mainly focus on the hydrothermal mineral assemblage in fractures. However, the evolution mechanisms of MHF during the mixing stage with connate fluid and lake bottom water remain unclear, and the complete "water-rock" reaction sequence of hydrothermal liquids is lacking.

The evolution of Paleoproterozoic shales in the Huanghua Depression within the Bohai Bay Basin aligns with the activation of Lanliao deep fault during the Paleocene-Early Eocene period (Zhang et al., 2011; Ye, 2013; Luo et al., 2017; Cheng et al., 2022). Previous studies identified multiple phases of MHF activities within the stratigraphy using hydrothermal mineral primary fluid inclusion homogeneous temperatures, Laser ablation spectroscopy of solid organic matter, and chlorite thermometers (Song et al., 2015; Lin et al., 2017; Han et al., 2021). These work also determined the affinity between hydrothermal fluids and MHF by comparing the standardized partition curves of REEs (Guo et al., 2016; Cheng et al., 2018; Zheng et al., 2018; Yang et al., 2018; Ma et al., 2020). Despite the determination of the source and activities period of these hydrothermal fluids, the mode is rarely discussed. The primary challenge lies in the absence of an indicator mineral that can stably exist across various active environments and evolutionary stages of hydrothermal fluids.

Previous studies have demonstrated a strong correlation between analcime formation and factors such as climate, paleoenvironment, and hydrothermal activity (Do Campo et al., 2007; English, 2001; Gall and Hyde, 1989; Keller, 1952; Sanchez-Valle et al., 2005; Savage et al., 2007; Bristow and Milliken, 2011; Varol, 2020; McHenry et al., 2020). Furthermore, analcime in shales has been reported to be related to reservoir development(Zhu et al., 2012; Iijima, 2001; Iijima and Hay, 1968; Bradley, 1928, 1929; Cole and Picard, 1978; Zhang et al., 2015; Ma et al., 2020). The integration of analcime with other minerals can be attributed to the thermodynamic equilibrium resulting from hydro-chemical alterations and kinetically controlled non-equilibrium dissolution (Iijima, 2001; Chipera et al., 2008). Analcime formed in high-alkalinity magmatic hydrothermal environments is distinguished by the enrichment of LILEs compared to interbedded mudstones, which may serve as a basis for identifying MHF activities in shales (Li, 1992; Fang et al., 2020; Yang et al., 2020). The study found that the Paleocene shale in the Bohai Bay Basin recorded the highest content of analcime (64.6%) in continental shales in China. The analcime consists of six types (occurring as laminae, lens, fracture filling, bioshell filling, vein marginal crystal and cement), and its distribution aligns with regional faults and magmatism in the plane, this suggests its potential as an indicator mineral for tracing hydrothermal fluid activity and evolution.

In this study, we conducted XRD, SEM, and LA-ICP-MA tests on samples from 10 wells in the Cangdong Sag of the Bohai Bay Basin. We performed extensive characterization and in situ chemical analysis of analcime carried out in micron-scale fractures and laminae. HFOA and CFOA are identified based on major elemental indicators (Si/Al, and 10K/(10K + Na)). The intensity and evolution stage of fluid activity were elucidated using to REEs and LILEs. In conjunction with the tectonic setting, we correlated the fluid evolution stage with the type of analcime, thereby constructing a comprehensive water-rock reaction sequence based on the formation model of analcime in hydrothermal systems. This research provides a new perspective on the micron-scale fluid tracing and evolution of shale in the faulted lake basins.

2. Geological setting

The Bohai Bay Basin is an extensional (rift) basin developed on the basement of the Paleozoic North China Craton. Its formation was caused by the subduction of the Pacific plate to the Eurasian plate, the northward push and collision of the Indian plate, and the impacts of thermal diapirism of the continental plates (Fig. 1A) (Liang et al., 2016; Dmitrienko et al., 2016; Zhao et al., 2019; Wu et al., 2020; Wang et al., 2022). The Cenozoic tectonic activity in the central structural belt of the Bohai Bay Basin was primarily governed by the dextral strike-slip of the Tanlu and Lanliao Faults, as well as their pull-apart effect. During the Paleocene-early Eocene period (the Kongdian Fm-Mbr 4 of the Shahejie Fm depositional period), the Pacific Plate's subduction and retreat in the SE direction led to a stress field extending NW-SE across eastern China. This induced the upwelling of deep materials and large-scale extensional tectonics, reactivating the Lanliao Fault that had formed during the Mesozoic. Furthermore, the subduction direction of the Pacific Plate to the Eurasian Plate changed from NW to near-EW during the middle Eocene (Mbr 3 of the Shahejie Fm -Mbr 2 of the Shahejie Fm depositional period) (Zhang et al., 2011; Ye, 2013; Luo et al., 2017; Cheng et al., 2022), which promoted the southward extension of the dextral activities of the Tanlu Fault zone and activation of the Lanliao Fault (which traverses the central section of the Bohai Bay Basin). The lithosphere of the North China Craton underwent significant destruction (Luo et al., 2017; Cheng et al., 2022), and this disruption was primarily attributed to a shear-stress component that triggered the dextral movement of the NE strike-slip fault zone within the Cangdong Sag. The accelerated westward subduction of the Pacific Ocean into the Eurasian continent during the Oligocene (Mbr 1 of the Shahejie Fm-the Dongying Fm depositional period) has led to the intensified dextral activity within Tanlu and Lanliao Fault zones. Consequently, the positive extension of the central structural belt in the Bohai Bay Basin has been significantly attenuated, whereas the impact of the strike-slip component has sharply intensified. At present, the Cangdong Sag functions as a secondary structural unit situated between the Kongdian, Dongguang, Xuhei, and Cangxian Uplifts in the southern region of the Huanghua Depression (Fig. 1A and B). From a planar perspective, the sag exhibits a trumpet-like morphology, diverging in the NE and converging in the SW. Its area is approximately 1760 km^2 (Yang et al., 2009; Cheng et al., 2018; Zhao et al., 2019; 2019b). Multiple transfer faults have developed within this region (Jiang et al., 2015; Pu et al., 2016).

The strata in the Cangdong Sag, arranged chronologically, comprise the Paleogene Kongdian, Shahejie, and Dongying Formations; Neogene Guantao and Minghuazhen Formations; and Quaternary Pingyuan Formation (Luo et al., 2017; Li et al., 2021; Xin et al., 2022) (Fig. 2). The Kongdian Formation is 2000–3000 m thick. This study primarily focuses on the second member from the Kongdian Formation, which is distributed over an area of approximately 500 km^2 and has a thickness ranging from 400 to 600 m. It predominantly consists of clayey and calcareous shale, along with dolomite (Fig. 2). During this period, the Cangdong Sag was in the sag stage, governed by initial rifting, and underwent minor tectonic activities. The primary depositional environment was an oxygen-depleted semi-deep to deep lake. The climate during this formation was relatively dry with high paleo-salinity levels (Zhao et al., 2018; Zhao et al., 2019; Li et al., 2020).

3. Methods

The materials used in this study includes 500m of drill cores and 119 samples of thin sections from ten wells (GX1、GX2、GX3、GD1、GD2、GD3、GD4、GD5、GD6、GD7). The data generated include 73 field emission scanning electron microscope (FESEM) samples, laser ablation inductively coupled plasma mass spectrometry (LA-ICP-MS) analysis of 11 samples, and X-ray diffraction (XRD) analyses of 2081 samples.

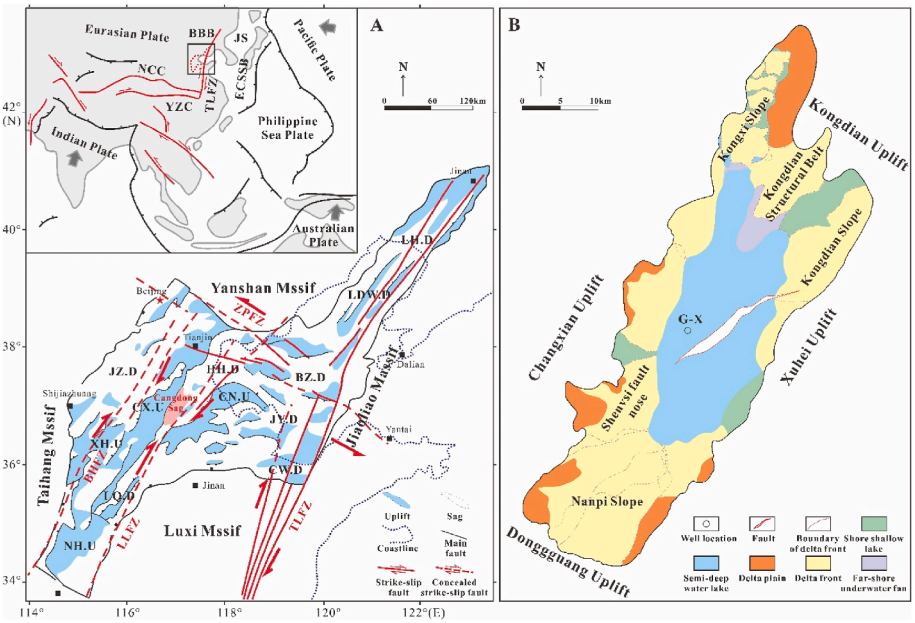

Fig. 1. Tectonic map of the Bohai Bay Basin and the Cangdong Sag. A. Sketched structural map of the Cenozoic BBB (revised from Wang et al., 2022). The Inset map shows the position of the BBB and plate interactions around the Eurasian Plate. Abbreviations: JS-Japan Sea; ECSSB-East China Sea Shelf Basin; JZ.D-Jizhong Depression; HH.D-Huanghua Depression; LQ.D-Linqing Depression; LH.D-Liaohe Depression; BZ.D-Bozhong Depression; LDW.D-Liaodongwan Depression; JY.D-Jiyang Depression; CX.U-Cangxian Uplift; XH.U-Xunheng Uplift; NH.U-Neihuang Uplift; CN.U-Chengning Uplift; DY.S-Dongying Sag; QD.S-Qingdong Sag; WB.S-Weibei Sag; LZW.SLaizhouwan Sag; B. Simplified structural map of the regional setting of the Cangdong Sag (modified after Zhao et al., 2018; Xin et al., 2022).

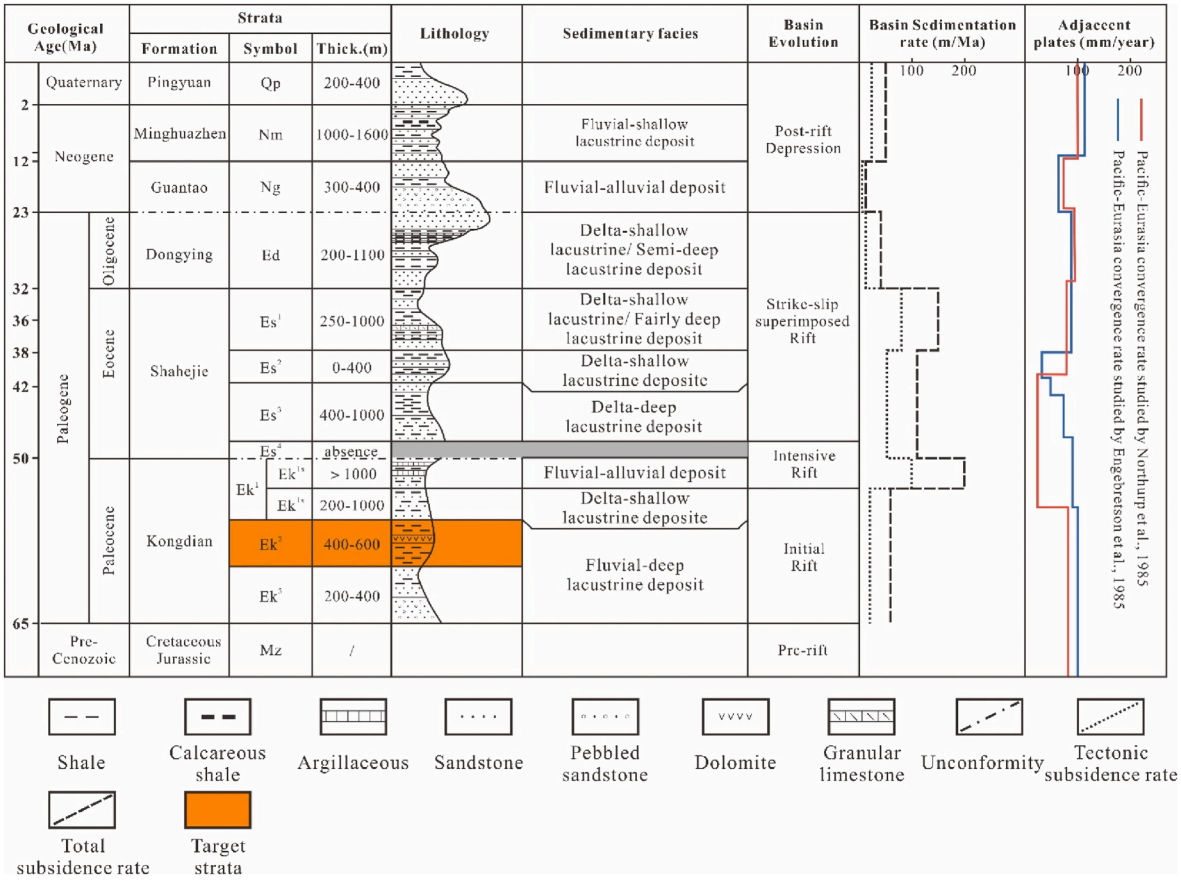

Fig. 2. Cenozoic strata and basin evolution of the Cangdong Sag (modified after Ye, 2013; Liu et al., 2018; Cheng et al., 2022).

3.1. X-ray diffraction analysis

The mineralogical analysis of the samples was performed using XRD at the State Key Laboratory of Heavy Oil Procession, China. Initially, the samples were powdered to a 200 mesh using an agate mortar. Analysis was undertaken using an X'pert Pro MPD with CuKα at 40 kV, 40 mA, a mineral diffraction angle (2θ) step width of 0.016°, and a 2θ measuring range of 5–60°. The mineral compositions were determined by computer analysis of diffractograms. Following this, the weight percentages of each identified mineral were quantitatively calculated.

3.2. Scanning electron microscopy

The SEM analysis was conducted at the China University of Petroleum (East China), using a Zeiss Crossbeam 550 SEM, which is integrated with a Bruker energy dispersive X-ray spectroscopy (EDS) XFlasher Detector 430-M analysis system. The EDS scanning resolution for this particular system is 20 μm. The observations of the SEM images were conducted on carbon-coated, freshly prepared shale samples that have been glued to aluminum stubs. The operating conditions employed included an extra high tension (EHT) of 10 kV and a 1 probe setting of 2.0 nA.

3.3. Laser ablation inductively coupled plasma mass spectrometry analysis

The trace elements analysis of silicate minerals was conducted using LA-ICP-MS in the State Key Laboratory of Mineral Deposit Geochemistry, Institute of Geochemistry, Chinese Academy of Sciences. The laser ablation (LA) system is a GeoLasPro 193 nm ArF excimer laser, and the inductively coupled plasma mass spectrometry (ICP-MS) is an Agilent 7900. During the analysis, the laser operating frequency was 5 Hz, the energy density was 4–5 J/cm, and the beam spot was selected to be 32 μm and 44 μm depending on the sample. Prior to testing, the ICP-MS performance was optimized with SRM610, and the content measurement was derived through the multiple external standard method employing total normalization. The external standard is usually USGS glass (NIST610, NIST612, BCR-2G, BIR-1G, and BHVO-2G). CGSG-1 and CGSG-2 are used as quality control samples. The recommended values for the elemental content of these silicate glasses were based on the GeoReM database. The processing of the analytical data (including the selection of sample and blank signals, instrument sensitivity drift correction elemental content correction, and calculation) was done using the ICPMS Data Cal software.

4. Results

4.1. Mineral composition and lithofacies

More than 67% of the shales of the second member of the Kongdian Formation in Cangdong Sag exhibit a laminar structure (Fig. 3). These laminar units contain analcime, carbonate, clay, felsic, and organic laminae. Taking Well GX-1 as a representative example, the XRD results of 1080 samples indicate that the second member of the Kongdian Formation is mainly composed of carbonate minerals (proportion of content: 0%–95%; average content: 31.6%), feldspar (proportion of content: 0%–68%; average content: 19.2%), quartz (proportion of content: 1%–47%; average content: 17.7%), clay minerals (proportion of content: 1%–41%; average content: 15.0%) and analcime (proportion of content: 0%–59%; average content: 14.6%). Subsequent components include pyrite (proportion of content: 0%–42%; average content: 0.6%), and various carbonate minerals including ankerite (proportion of content: 0%–86%; average content: 20.5%), calcite (proportion of content: 0%–70%; average content: 8.1%), dolomite (proportion of content: 0%–95%; average content: 3.3%), along with feldspar including plagioclase (proportion of content: 0%–45%; average content: 13.0%) and potassium feldspar (proportion of content: 0%–23%; average content: 6.2%) (Fig. 3).

4.2. Analcime occurrence and assemblage

Field emission scanning electron microscopy and scanning of elemental distribution in micron-scale areas were used to detect and describe analcime in the shales of the second member of the Kongdian Formation. The analcime can be divided into six distinct types based on occurrence characteristics (occurring as laminae, lens, fracture filling, bioshell filling, vein marginal crystal and cement). Analcime laminae was further divided into ADML, ACL, A-CCL, and A-PML based on the component differences in the laminae and interlaminar patterns (Table 1).

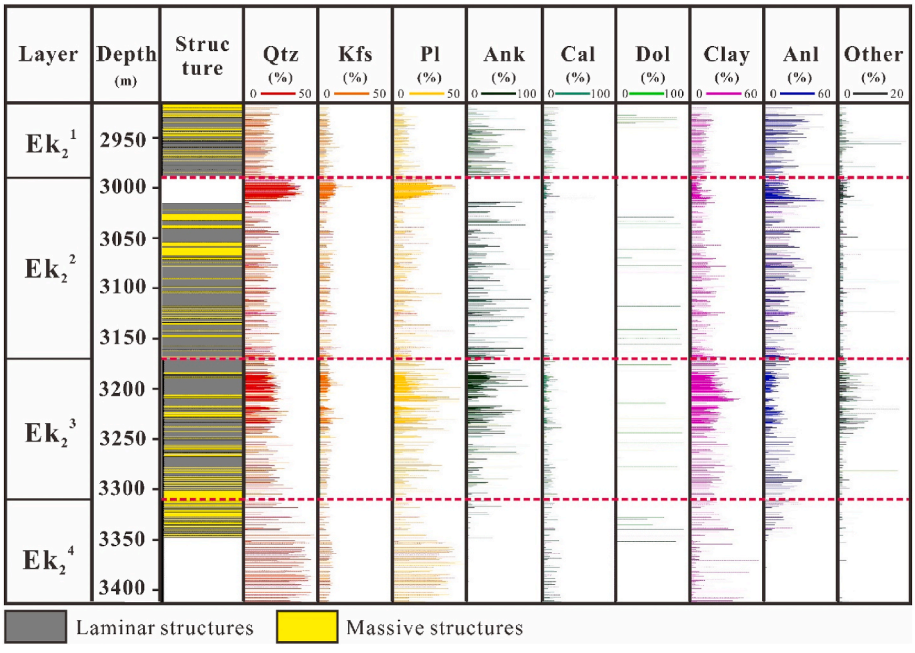

Fig. 3. Vertical variation of mineral content in GX-1 well of Ek2 in Cangdong depression of Bohai Bay Basin.

Table 1
Analcime classification table.

Occurrence		Thick of A-La.	Size of A-Gr.	Associated materials
Laminae	ADML	20–50 μm	3–10 μm	Dolomite, Calcite, Clay minerals
	ACL	20–50 μm	5–10 μm	Clay minerals
	A-CCL	20–80 μm	3–15 μm	Calcite, Clay minerals
	A-PML	40–300 μm	5–20 μm	Pyrite, Clay minerals
Filling	FFA	/	20–150 μm	Pyrite, Hydrocarbon
	BFA	/	3–10 μm	Pyrite, Hydrocarbon
Lens		/	10–25 μm	Clay minerals
Vein marginal crystal-VMA		/	50–300 μm	Calcite, Barite
Cement		/	/	K-feldspar, Albite, Plagioclase, Quartz, Pyrite

4.2.1. Analcime laminae

The study examines analcime laminae interbedded with carbonate minerals, clay, felsic, organic, and pyrite laminae in four distinct forms: (a) analcime laminae-dolomite laminae-mixed laminae (ADML); (b) analcime laminae-clay laminae (ACL); (c) "analcime + calcite laminae"-clay laminae (A-CCL); and (d) "analcime + pyrite laminae"-mixed laminae (A-PML) (Fig. 4).

4.2.1.1. Analcime laminae-dolomite laminae-mixed laminae (ADML). Analcime laminae develops between dolomite laminae and mixed laminae (Fig. 4A). Within analcime laminae, the content of analcime is more than 80% with a particle size of 3–10 μm. The calcite content was less than 15% with a particle size of 3–8 μm and corrosion mark on the surface (Fig. 4B).

4.2.1.2. Analcime laminae-clay laminae (ACL). In this assemblage, the analcime laminae was mostly distributed in the interlayer of the clay laminae (Fig. 4D–E). The content of analcime within this layer exceeded 95%. The automorphic particles measured between 5 and 10 μm in size, with the interparticle spaces being filled by organic-rich clay minerals (Fig. 4F).

4.2.1.3. "Analcime + calcite" laminae-clay laminae (A-CCL). Analcime and calcite were found in the same laminae within the A-CCL assemblage (Fig. 4G–H). The size of analcime (3–15 μm) was slightly smaller than that of calcite (5–20 μm) (Fig. 4I). The clay laminae primarily comprised illite, interbedded with the "analcime–calcite" laminae (Fig. 4G–H).

4.2.1.4. "Analcime + pyrite" laminae-mixed laminae (A-PML). Analcime, when distributed within the A-PML assemblage, is either found in independent laminae or coexist with pyrite within the same laminae (Fig. 4J). Additionally, pyrite encapsulated granular analcime or in the form of radial needles (Fig. 4L–K).

4.2.2. Fracture filling analcime (FFA)

FFA is distributed along the fracture edges, ranging in size from 20 to 150 μm, while hydrocarbon fills the center. Unstable analcime laminae form from the fracture edges towards both sides, with an extension distance typically less than 200 μm (Fig. 5A–B).

4.2.3. Vein marginal crystal analcime (VMA)

VMA formed on the edges of hydrothermal mineralized veins which consist of calcite and barite. The analcime within the calcite veins exhibited a higher degree of automorphism and frequently fractured (Fig. 5C). In contrast, the analcime in the barite vein displayed an extreme automorphism towards the vein side, but the outlines on the side facing the substrate were not distinct. Within the core of the analcime, the residual substrate components could be observed, appearing circular and flaky under the microscopic examination (Fig. 5D).

4.2.4. Bioshell filling analcime (BFA)

BFA fills the bio-cavities or bio-debris sheltered spaces, along with dolomite, quartz, potassium feldspar, and clay minerals (Fig. 5E–F). The analcime transitioned from granular to cement-like fillings without any obvious particle shape (Fig. 5G). Pyrite is observed in the form of agglomerates or cuboids (Fig. 5H). Pyritization frequently occurred along the edges of intact algal calcareous shells, which have phosphorus-rich cores (Fig. 5I–J).

4.2.5. Analcime lens

Analcime lens predominantly presented as an elliptical and lenticular aggregates oriented in one direction (Fig. 5K). Clay minerals filled the interparticle spaces of analcime (Fig.5L).

4.2.6. Analcime cement

Analcime cement and pyrite cement jointly functioned as cement to fill the spaces between silty detrital particles (Fig. 5M–N). The concentration of analcime was notably higher in areas where the detrital particles were predominantly located (Fig.5M). These detrital particles included quartz, potassium feldspar, and plagioclase. Notably, the quartz surfaces were extensively eroded, while the potassium feldspar exhibited enlarged rims during the later stages (Fig.5O).

4.3. Geochemical characteristics

4.3.1. Major elements

In-situ laser ablation experiments were conducted to detect the major elements. The results showed that the Si/Al range of analcime was 2.17–2.64, (average: 2.44). The main components included Na_2O, Al_2O_3, and SiO_2; others included MgO, K_2O, CaO, MnO, and FeO (Table 2). Analcime laminae (ACL, A-CCL, and A-PML) exhibited low Na_2O and Al_2O_3 contents but high MgO, K_2O, and CaO contents. A-CCL and A-PML had higher FeO contents compared to ACL. FFA and VMA contained high Na_2O and Al_2O_3 contents but a negligible amount of MgO, K_2O, and CaO. The Na_2O contents of BFA and analcime lens were similar to that of FFA and VMA, but the Al_2O_3 contents were slightly lower. The MgO, K_2O, and CaO contents were higher than that of FFA, VMA, and analcime cement, but lower than that of analcime laminae (ACL, A-CCL, and A-PML).

4.3.2. Trace and rare earth elements

The enrichment of trace elements in analcime laminae (ACL, A-CCL, A-PML) was significantly higher than that observed in FFA, BFA, VMA, analcime lens, and analcime cement (Fig. 6A–B). Among these, A-PML exhibited the higher enrichment with large-ion lithophile and siderophile elements than ACL and A-CCL. There were obvious differentiations of Co, Ni, Cu, Zn, Pb, and Bi (Fig. 6A). In the case of ACL, the enriched large-ion lithophile and siderophile elements were Co and Ni, whereas the other elements were mostly depleted (Fig. 6A). In contrast, the elements in A-CCL were mostly depleted, except for the siderophile elements and Mo, which were enriched (Fig. 6B). There was a strong and consistent trend of Cs enrichment in FFA, BFA, analcime lens, VMA and analcime cement. However, the enrichment of the other elements was substantially varied, although most of them were obviously depleted compared to the upper crust. This trend is significant but not the main focus of analysis due to the overall low contents of trace elements in FFA, BFA, analcime lens, VMA and analcime cement.

The concentration of REEs in the analcime from the second member of the Kongdian Formation was low, ranging from 0.0582 to 31.7720 ppm. This average concentration of REEs of the six analcime occurrence types were much lower than that of (i) the post-Archean shale in Australia (184.77 ppm) and (ii) the upper continental crust (UCC)

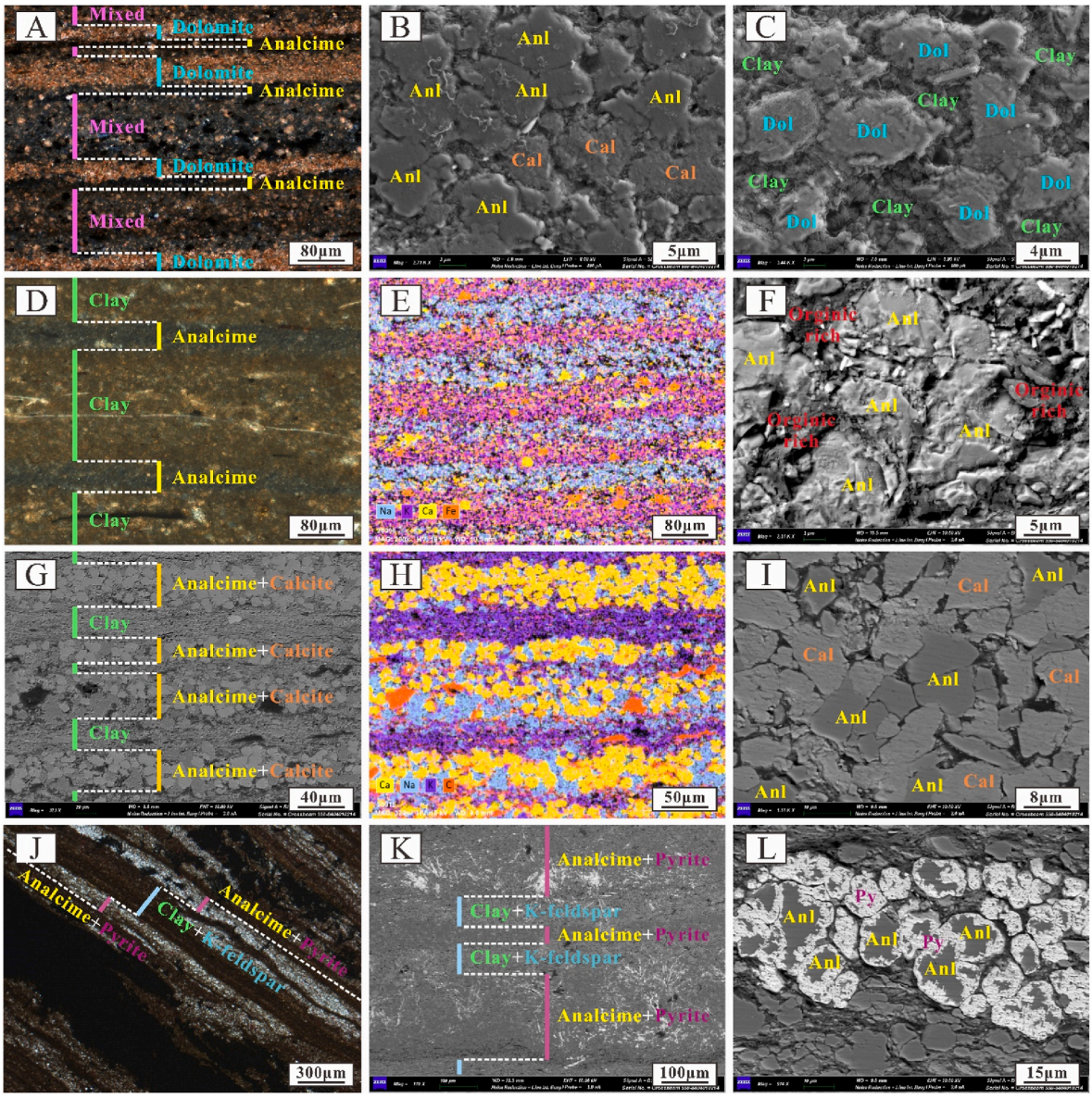

Fig. 4. Occurrence characteristics of laminar analcime A. analcime lamina-dolomite lamina-mixed lamina, (ADML) (GX 3284m); B. the internal structure of the analcime lamina in ADML, there is no fixed morphology of analcime and calcite, and the surface dissolution of calcite is obvious (GX 3284m); C. the internal structure of the dolomite lamina in ADML, the dolomite is pelleted, filled with clay minerals between grains, the surface has corrosion marks (GX 3284m); D. analcime lamina-clay lamina, (ACL)(GX 2931m); E. microscopic element distribution of ACL (GX 3180m); F. the internal structure of the analcime lamina in ACL, analcime is filled with organic-rich clay minerals (GX 3180m); G. "analcime + calcite lamina"-clay lamina, (A-CCL) (GX 3241m); H. microscopic element distribution of A-CCL (GX 3241m); I. the internal structure of the analcime lamina in A-CCL; J. "analcime + pyrite lamina"-mixed lamina, (A-PML)(GX 3374m); K. analcime + pyrite lamina-mixed lamina, (A-PML)(GX 3119m); L. analcime is wrapped by pyrite (GX 3119m).

(146.4 ppm) (Table 2). The chondrite-normalized curve presented an obvious right-sloping trend (Fig. 7), with moderate differentiation in the light REEs among ACL, A-CCL, A-PML, BFA, and analcime lens. However, no obvious differences were observed among the occurrence types for heavy REEs. The Ce content was normal, while Eu depletion was obvious in all Analcime types except analcime cement (Table 3). The REE contents in FFA, VMA, and analcime cement were too low to be accurately calculated.

5. Discussion

5.1. Analcime origin

The Si/Al ratio in analcime within the study area ranges from 2.17 to 2.74, with a majority distribution between 2.2 and 2.5. This corresponds to non-tuffaceous source in saline lake and hydrothermal depositional genesis according to the Si/Al classification scheme proposed by Coombs and Whetten (1967) (Fig. 8). However, no reliable analysis has been proposed to classify these causes beyond combining microscopic petrological features. Based on in-situ quantitative elemental tests, this research distinguishes analcime with different genesis in low to medium Si/Al (2.2–2.5), providing a basis for discussing the fluid tracing ability of analcime.

Previous studies have shown that 10K/(10K + Na) can be used to indicate hydrothermal fluid activities (Giggenbach, 1988; Boschetti et al., 2022). Analcime can be further divided into HFOA and CFOA based on origin (Fig. 9). CFOA contain three types analcime laminae (ACL, A-CCL, and A-PML), the 10K/(10K + Na) of these analcime laminae (0.27–0.82) is close to the shale of the Kongdian Fm (0.41–0.93), high K content may be influenced by clay minerals and

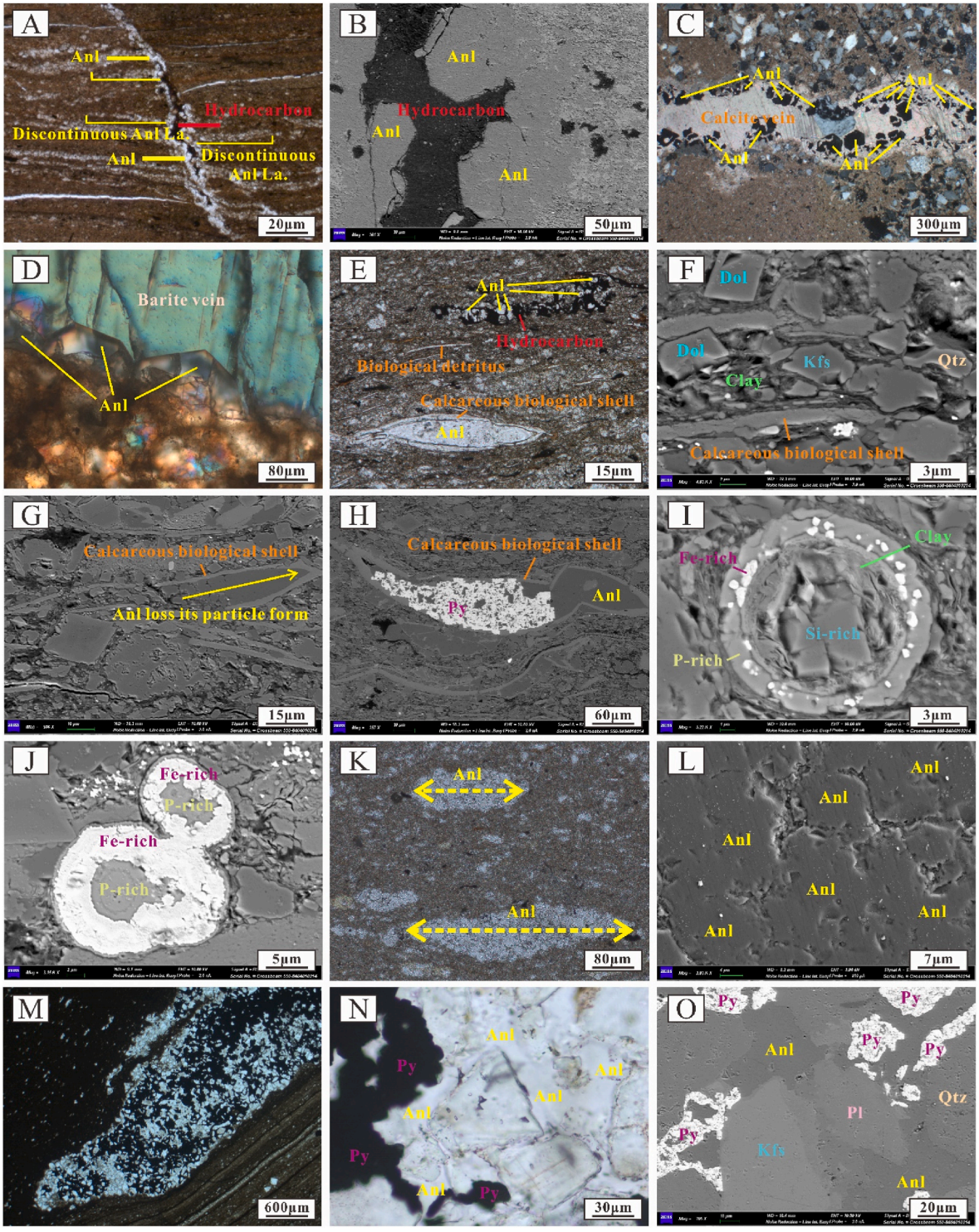

Fig. 5. Occurrence characteristics of FFA, BFA, analcime lens, VMA, and analcime cement A. fracture filled with analcime and hydrocarbon materials, analcime laminae are derived on both sides of the fracture with poor continuity (GX 3180m); B. fracture filled with analcime and hydrocarbon materials, from horizon A (GX 3180m); C. analcime particles formed at the edge of calcite vein (GD 3810m); D. analcime particles formed at the edge of barite vein (GD 3810m); E. analcime, pyrites, and organic matter coexisted in intact shells (GX 2932m); F. the sheltered spaces were filled with dolomite, quartz, potassium feldspar, and clay minerals (GX 2932m); G. the analcime transitioned from granules to the shape of cement fillings without any obvious particle shape (GX 2932m); H. analcime, pyrites, and organic matter coexisted in intact shells, the pyrite was in the shape of agglomerates or cuboids (GX 2938m); I. pyritization occurs in the shell of algal fossils (GX 2932m); J. phosphorus-rich algal fossils are pyritized, pyrite is distributed in annular zones with concentric ring structure (GX 2932m); K. analcime lens predominantly presented as elliptical and lenticular aggregates oriented in one direction (GX 3018m); L. analcime lens had a clear outline (GX 3018m); M. distribution of analcime cement (GX 3379m); N. analcime cement and pyrite jointly acted as cement to fill the spaces between silty detrital particles (GX 3379m); O. distribution characteristics of cement and clastic particles (GX 3379m).

Table 2
In-situ major elements of analcime in Ek2 of Cangdong Sag.

SAMPLE	Na_2O	MgO	Al_2O_3	SiO_2	P_2O_5	K_2O	CaO	MnO	FeO	Si/Al	TYPE
S10	11.2525	0.3427	19.0707	59.188	0.0045	0.4897	1.1894	0.0113	0.3965	2.64	**ACL**
S10	10.6895	1.1659	17.766	51.0487	0.0175	0.5418	7.3767	0.0812	2.6804	2.46	**ACL**
S10	11.4504	0.7375	17.3789	55.4528	0.0116	0.5564	3.7901	0.0462	0.4776	2.43	**ACL**
S10	11.0489	0.6605	19.0986	56.6698	0.0115	0.9651	2.6397	0.0238	0.7669	2.52	**ACL**
S10	12.2146	0.1643	20.0785	58.3452	0.0044	0.4239	0.2988	0.0022	0.4264	2.47	**ACL**
S10	11.9742	0.3279	19.5542	56.2966	0.0084	0.4009	1.4562	0.0161	1.7374	2.45	**ACL**
S10	11.6911	0.5118	19.8235	57.3338	0.015	0.5728	1.4742	0.0221	0.4921	2.46	**ACL**
S10	10.9251	1.1501	18.3987	54.5573	0.013	0.6681	4.4284	0.0641	1.6308	2.52	**ACL**
S10	11.1282	0.6346	18.0317	56.0531	0.0029	0.7743	2.3972	0.0301	2.7697	2.64	**ACL**
S8	9.5576	1.025	19.1515	57.3988	0.0175	2.0406	1.4678	0.0211	1.1938	2.55	**A-CCL**
S8	10.4352	0.733	19.3979	57.5821	0.0377	1.2453	1.3434	0.1693	1.1141	2.52	**A-CCL**
S8	10.7796	0.3666	19.6207	59.2063	0.0464	0.8159	0.5389	0.0046	0.5621	2.56	**A-CCL**
S8	10.2142	0.3857	18.9562	58.327	0.0277	1.6032	1.9194	0.0099	0.469	2.62	**A-CCL**
S8	10.2406	0.4003	18.8157	60.5493	0.0101	0.9451	0.3131	0.0055	0.659	2.74	**A-CCL**
S8	10.9632	0.4713	20.1562	58.051	0.0551	1.1662	0.3384	0.0054	0.7219	2.45	**A-CCL**
S8	10.8594	0.3976	20.2465	58.2489	0.0316	1.0728	0.3885	0.0046	0.6837	2.45	**A-CCL**
S8	10.1232	0.6958	19.2566	58.5073	0.0268	1.3517	0.8283	0.014	1.1025	2.58	**A-CCL**
S8	9.4157	0.8629	19.0601	58.4117	0.5677	1.4949	1.15	0.017	1.4078	2.6	**A-CCL**
S8	9.9959	0.7234	19.4088	58.3721	0.0333	1.4632	0.9324	0.009	0.964	2.56	**A-CCL**
S12–2	11.831	0.2898	20.8857	57.4827	0.0482	0.874	0.0162	0.0017	0.5027	2.34	**A-PML**
S12–2	12.04	0.2008	20.6731	57.7413	0.0539	0.8401	0.0465	0.0014	0.3541	2.37	**A-PML**
S12–2	11.6145	0.2705	20.6624	57.9076	0.0325	0.9666	0	0.0015	0.4581	2.38	**A-PML**
S12–2	11.0641	0.4149	20.5717	57.9407	0.038	0.123	0.0531	0.0027	0.7132	2.39	**A-PML**
S12–2	11.4653	0.3376	20.3298	58.1756	0.0386	0.9865	0.0471	0.0018	0.5404	2.43	**A-PML**
S12–2	10.1732	0.471	19.8382	58.821	0.1087	1.5864	0.1256	0.0031	0.7775	2.52	**A-PML**
S12–2	10.3971	0.4048	20.2146	57.947	0.1211	2.0065	0.1253	0.0033	0.6634	2.44	**A-PML**
S12–2	10.0489	0.5817	19.8867	59.9507	0.14	2.0269	0.1707	0.004	1.0707	2.48	**A-PML**
S12–2	10.1423	0.4497	19.9037	58.5952	0.1315	1.7523	0.1613	0.0039	0.764	2.5	**A-PML**
S12–2	10.2227	0.4581	19.6836	58.7576	0.1136	1.7231	0.1962	0.0029	0.7496	2.54	**A-PML**
S12–1	13.5113	0.0002	20.4741	58.0081	0	0.0034	0	0	0	2.41	**FFA**
S12–1	13.4457	0.0002	20.3691	58.1786	0	0.0034	0	0	0	2.43	**FFA**
S12–1	13.2171	0.1969	20.426	58.2825	0	0.0091	0.0228	0.0008	0.0178	2.43	**FFA**
S12–1	13.4792	0.0037	20.6681	57.8314	0	0.0104	0	0.0002	0.0004	2.38	**FFA**
S12–1	13.4679	0.0007	20.8355	57.6897	0	0.0035	0	0	0	2.35	**FFA**
S12–1	13.4119	0.0002	20.6793	57.9018	0	0.0039	0	0	0	2.38	**FFA**
S12–1	13.7195	0.0035	20.5146	57.7457	0	0.0064	0	0.0001	0.007	2.39	**FFA**
S12–1	13.3514	0.0005	20.4702	58.1713	0	0.0039	0	0	0	2.42	**FFA**
S12–1	13.2414	0.0009	20.2615	58.4868	0	0.0067	0	0	0	2.45	**FFA**
S3180	13.1469	0.0001	21.7668	57.061	0.0036	0.007	0	0	0.0072	2.23	**VMA**
S3180	13.1352	0.001	21.849	56.9882	0	0.0091	0.002	0.0002	0.0079	2.22	**VMA**
S3180	13.1267	0.0002	21.6171	57.2245	0.0023	0.0007	0	0.0004	0.0127	2.25	**VMA**
S3180	12.8911	0	21.8731	57.2126	0	0.0088	0	0.0004	0.0074	2.22	**VMA**
S3180	13.155	0.0022	21.725	57.0895	0.0021	0.0091	0	0.0002	0.0104	2.23	**VMA**
S3180	13.1933	0.0002	22.1575	56.6287	0.0017	0.0069	0	0	0.0053	2.17	**VMA**
S3180	13.0011	0.0002	21.9454	57.0178	0.0047	0.0072	0.013	0.0008	0.0041	2.21	**VMA**
S3180	12.9431	0.0001	21.88	57.0178	0.0032	0.0071	0.0042	0	0.006	2.22	**VMA**
S9	13.0848	0.053	20.1929	58.4465	0.0076	0.0783	0.0372	0.0009	0.0874	2.46	**BFA**
S9	13.1115	0.0438	20.0997	58.4642	0.0264	0.1002	0.0691	0.0014	0.0747	2.47	**BFA**
S9	13.1774	0.1179	19.7316	58.4895	0.0026	0.0887	0.1432	0.0031	0.2307	2.52	**BFA**
S9	16.5256	0.0396	20.4008	57.8213	0.008	0.0584	0.0957	0.0011	0.0407	2.41	**BFA**
S9	13.0761	0.1264	19.9572	58.4077	0.0077	0.0917	0.1875	0.0024	0.1306	2.49	**BFA**
S12–1	12.8891	0.0716	20.6235	57.8949	0.0006	0.2518	0.0944	0.0016	0.1236	2.39	**lens**
S12–1	12.9348	0.1023	20.4244	57.6664	0.0247	0.2532	0.0978	0.0024	0.4415	2.4	**lens**
S12–1	13.2435	0.4222	20.1889	56.7721	0.0252	0.1878	0.7424	0.0121	0.3399	2.39	**lens**
S12–1	12.4622	1.038	19.6769	55.005	0	0.2787	0.6996	0.0314	2.6555	2.38	**lens**
S12–1	13.2377	0.1527	20.3951	57.5933	0.0096	0.0839	0.2532	0.0033	0.1911	2.4	**lens**
S12–1	12.7476	0.3095	20.4573	57.3942	0.0248	0.1644	0.4991	0.0083	0.3057	2.38	**lens**
S4-2	11.8212	0.0215	20.1321	59.7809	0.0019	0.1618	0.02	0	0.0494	2.52	**cement**
S4-2	12.373	0.0021	20.5698	59.024	0.0016	0.0144	0.0041	0	0.0003	2.44	**cement**
S4-2	8.9926	0.006	20.8096	58.5934	0.0001	0.2762	3.0258	0.0003	0.0734	2.39	**cement**

alkaline connate fluid. HFOA contain VMA, analcime cement, analcime lens and two types of analcime filling (FFA and BFA), the 10K/(10K + Na) value of HFOA is lower than 0.24. Among HFOA, the FFA and VMA have the lowest 10K/(10K + Na) value (<0.04), this reflect the dominant role of MHF during their formation. Furthermore, FFA and VMA possess excellent mineral morphology and commonly coexist with hydrothermal minerals such as calcite and barite, which provides petrographic evidence that FFA and VMA originated from hydrothermal fluids. The value of 10K/(10K + Na) of BFA (0.02–0.11) and analcime cement (0.01–0.15) is higher than FFA and VMA but lower than analcime lens (0.14–0.21). Although the 10K/(10K + Na) of BFA and analcime cement are relatively similar, the petrological characteristics indicate differences in their K sources. Analcime cement existed as interparticle cement together with pyrite, (Fig. 5M-O). Pyrite was enriched with Mo and other characteristic trace elements that represented high-temperature alkaline hydrothermal fluids, suggesting that these fluids were alkaline and rich in K and Na under a reducing environment. Thus, it is plausible that analcime cement contains high K contents. BFA was formed within biological shell or inside their sheltered spaces, some of the BFA was in direct contact with the clay minerals in the original components and the resultant effect might be high K contents. Although the enrichment mechanisms of these two types are

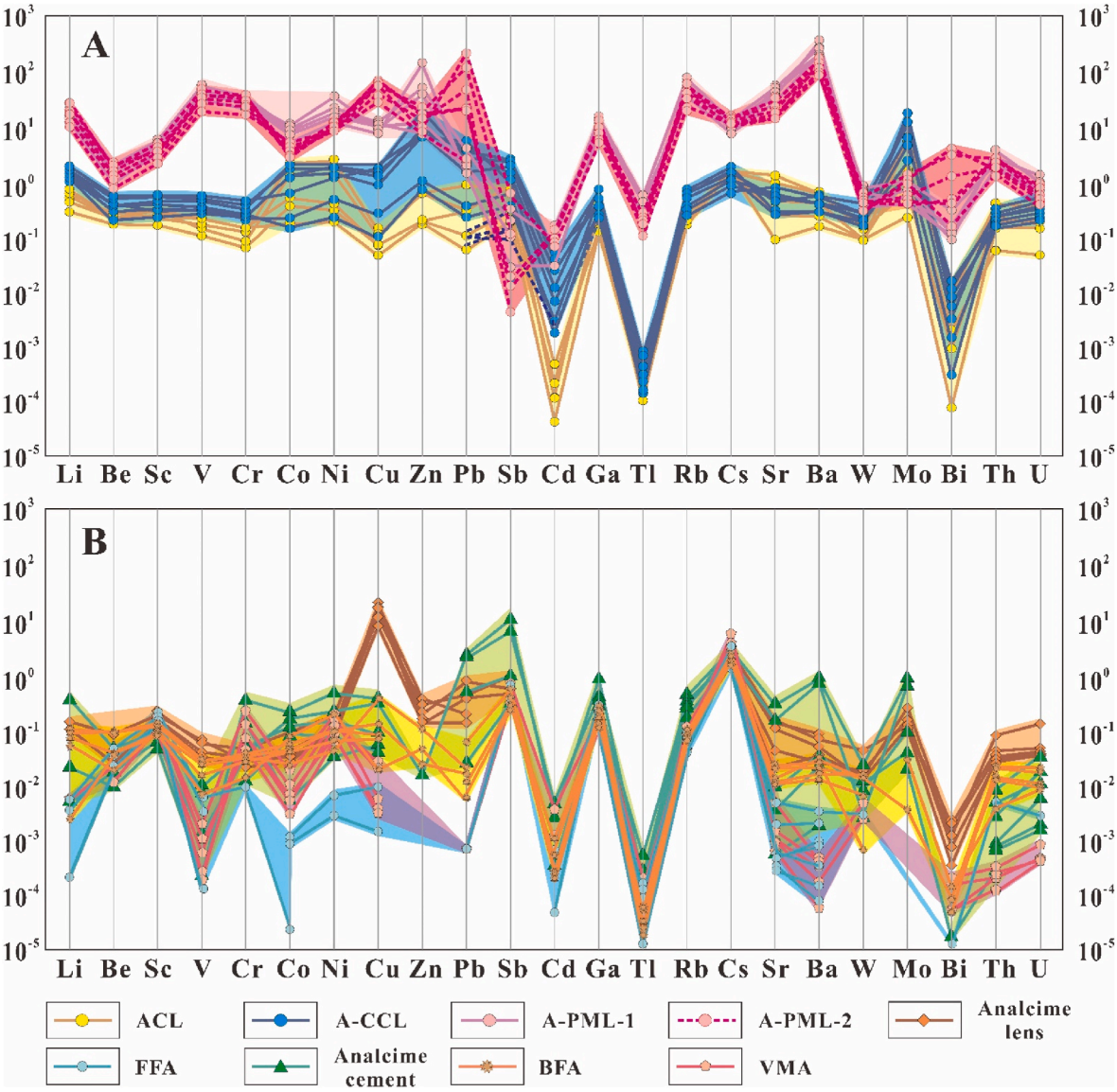

Fig. 6. Spider web diagram of standardized trace elements of analcime in Ek2 of Cangdong Sag A. Spider web diagram of standardized trace elements of analcime laminae (ACL + A-CCA + A-PML); B. Spider web diagram of standardized trace elements of FFA, BFA, analcime lens, vein marginal crystal analcime, and analcime cement.

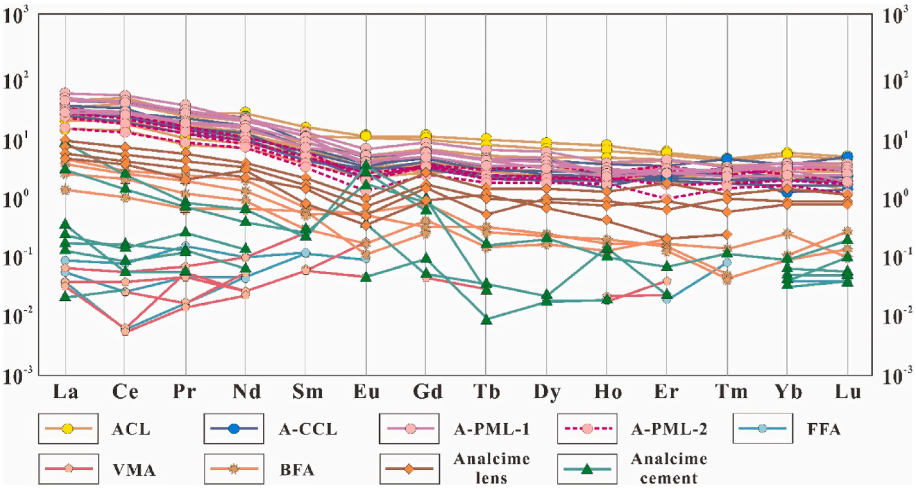

Fig. 7. Chondrite-normalized curve of analcime in Ek2 of Cangdong Sag.

Table 3
In situ Rare Earth Elements of analcime in Ek2 of Cangdong Sag.

TYPE		∑REE	∑LREE	∑HREE	L/H	$(La/Yb)_N$	$(Ce/Yb)_N$	$(La/Sm)_N$ (Gd/Yb)N	$(Gd/Yb)_N$	δCe	δEu
ACL	MAX	63.5168	56.1983	7.3185	10.4839	13.4654	9.5779	4.4163	2.0366	1.4171	0.9848
	MIN	10.0321	9.1585	0.8736	6.1566	6.1351	5.9028	2.6356	1.0582	0.7516	0.623
	AVE	31.5686	28.1018	3.4668	8.4547	8.4248	7.1717	3.6053	1.5091	1.2283	0.7389
A-CCL	MAX	42.5473	39.1077	3.4396	16.1162	27.8653	23.7318	7.5379	3.5454	1.2034	1.1528
	MIN	12.864	11.7943	1.0697	9.9446	9.7546	6.6093	4.5377	0.8287	0.9636	0.4903
	AVE	27.021	24.9555	2.0656	12.2199	16.2887	12.802	5.2928	2.276	1.0657	0.7369
A-PML	MAX	52.485	49.6381	4.2862	17.436	24.4416	21.9847	6.1046	2.9268	1.243	1.0603
	MIN	15.7842	14.3313	1.4529	9.8637	7.7693	6.6674	3.5651	0.9511	0.978	0.4166
	AVE	31.772	29.1948	2.5771	11.2249	12.1576	9.96	4.6073	1.6054	1.0666	0.6898
FFA	MAX	0.0565	0.6472	0.0285	5.2427	/	/	/	/	/	/
	MIN	0.0121	0.0004	0	0.4872	/	/	/	/	/	/
	AVE	0.0672	0.053	0.0142	3.8407	/	/	/	/	/	/
VMA	MAX	0.1361	0.1275	0.0161	14.8438	/	/	/	/	/	/
	MIN	0.0279	0.022	0.0041	1.4797	/	/	/	/	/	/
	AVE	0.0582	0.0502	0.008	7.2705	/	/	/	/	/	/
BFA	MAX	3.8633	0.6045	0.0296	22.4903	24.218	20.9836	8.2499	4.6225	1.2178	1.0066
	MIN	1.2986	0.1994	0.0128	15.5938	14.1858	9.5291	2.1592	1.4205	0.5465	0.2695
	AVE	2.7803	0.4322	0.0234	18.1683	18.3282	13.0387	5.16	3.0536	0.9439	0.6331
Analcime lens	MAX	13.028	12.1128	1.4657	13.2356	12.0917	9.7495	9.9451	3.0937	1.1698	1.0439
	MIN	3.763	3.3871	0.3759	5.3727	5.53	4.282	1.9607	1.2721	0.8438	0.349
	AVE	7.1725	6.4217	0.7508	9.2353	8.9564	6.8331	4.7265	1.7611	1.0433	0.6078
Analcime cement	MAX	4.0815	3.9118	0.2412	23.048	/	/	/	/	/	/
	MIN	0.0434	0.0224	0.0052	1.07	/	/	/	/	/	/
	AVE	1.4508	1.3744	0.0764	9.675	/	/	/	/	/	/

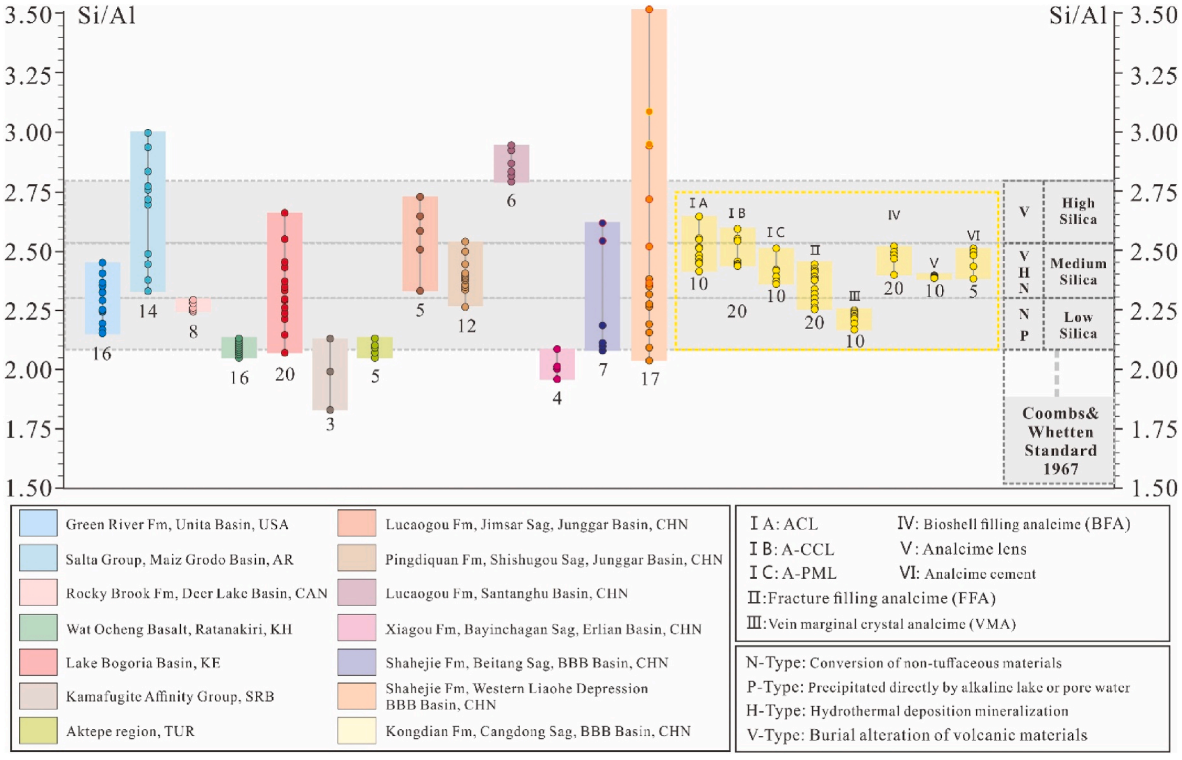

Fig. 8. Si/Al ratio comparison of analcime distributed in shale analcime.

different, there were good corresponding relationships with the information provided by their occurrences (Fig. 5K-L). Analcime lens has the highest 10K/(10K + Na) value in HFOA, it was entirely surrounded by clay minerals. The concentrated appearance of analcime lens forms weak layering characteristics, which are most similar to ACL in CFOA, their 10K/(10K + Na) are also closest to each other.

Considering these differences, the analcime with six occurrence types can be divided into two origin: (i) HFOA, consisting of FFA, BFA, analcime lens, VMA, and analcime cement; and (ii) CFOA, comprising ACL, A-CCL, and A-PML.

5.2. Fluid tracing and evolution

As previously noted, the stress field of the Bohai Bay Basin stretched in the NW-SE direction during the Paleocene-early Eocene period (specifically, the Kongdian Fm-Mbr 4 of the Shahejie Fm depositional period), causing the upwelling of MHF. The formation of the second member of the Kongdian Formation coincided with the activation time of the Lanliao Fault. Additionally, the Kongdian Formation was also connected to the concealed and downward deep fracture zone of the Huanghua-Dezhou-Dongming strike-slip structural belt, which

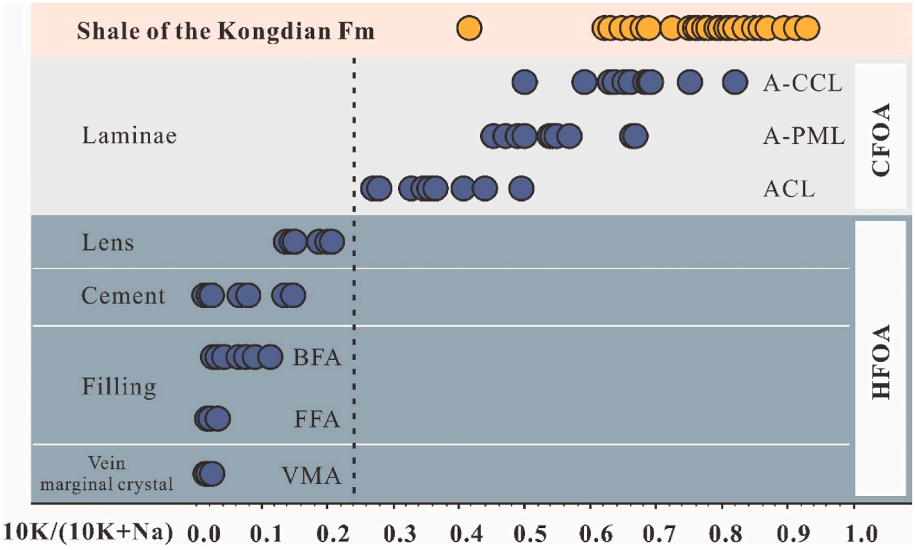

Fig. 9. The origin of analcime. CFOA: connate fluid origin analcime, HFOA: hydrothermal fluid origin analcime.

corresponded to the Lanliao Fault and traverses the central part of the Bohai Bay Basin. As it descends, the fracture zone can traverse the detachment plane of the extended tectonic system to reach the mantle. During the depositional and burial processes in the evolution of the second member of the Kongdian Formation, the Eocene activation of the Lanliao Fault and its Oligocene dextral intensification had dominant impacts on the formation of the NNE-NE trending fault groups in the Cangdong Sag. The cumulative effect of these concealed faults, along with the concealed fracture zone of the Huanghua-Dezhou-Dongming strike-slip structural belt and the abyssal Lanliao Fault, facilitated the connection between the deep mantle and the shallow buried diagenetic and sedimentary systems. The authors of previous studies have also suggested that various stages of Paleogene basalts in the Huanghua Depression originated from primary mantle-derived magma (Li et al., 2016; Wang et al., 2018). MHF from the deep mantle upwelled relied on deep faults as the migratory channels. In the process, characteristic minerals such as analcime, barite, calcite, pyrite, and anhydrite were precipitated (Bennett et al., 2008; Yang et al., 2020; Han et al., 2021).

In the second member of the Kongdian Formation, analcime distribute around faults, the closer to the fault, the higher the analcime contents, the stronger the impact of MHF (Fig. 10). In addition to the analcime formed in the Huanghua Depression (controlled by the Lanaliao Fault), analcime also developed in the Paleogene shale of the Liaohe Depression (controlled by the Tanlu Fault) (Sun et al., 2014; Song et al., 2015; Fang et al., 2020). Considering regional structure, magmatic activities, and the petrological information of analcime and their associated minerals, we propose that the upwelling of mantle-derived magma under the control of tectonic activities by abyssal faults was the decisive factor for analcime enrichment.

Han et al. (2021) reported the existence of complex mineral assemblages formed by hydrothermal activities in the mudstone fractures near the basaltic layer of the study area. The inclusions, observed at temperatures ranging from 84 °C to 354 °C, could potentially be attributed to a gradual crystallization process, transitioning from high to low temperatures during a multi-phase hydrothermal evolution. A possible sequence would be pyrobitumen-natrolite-chlorite-barite-calcite (only represents the order of formation, not the transformation relationship). In this process, the mineral species in the fluids reduced and gradually

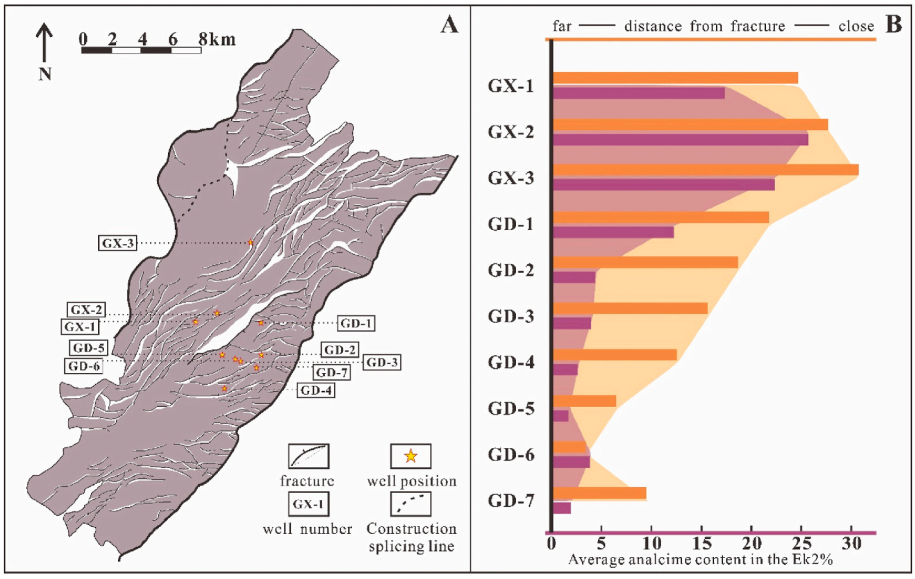

Fig. 10. Analcime content and fracture distribution in Cangdong sag. A. Structural map of Ek_2 bottom and distribution of sampling well locations (modified after Luo et al., 2017; Zhao et al., 2018); B. The distance between the sampling well and the fracture is negatively correlated with the content of analcime in the Ek_2.

became stable, and the degree of crystallization was more consistent.

Considering the preceding discussion, we propose that VMA and FFA might represent different stages of crystallization during the migration of MHF. VMA is generated from MHF near the magma, water-rock reactions caused the extremely automorphic analcime to be distributed along the edges of the veins. FFA is generated from MHF far from the magma. As the fluids migrated to the shallow part of the formation, the temperature and pressure decreased. Under the control of mineral dissolution-precipitation equilibrium, ions in the fluid crystallize to form calcite veins, barite veins, and analcime at depth, and form only analcime in shallow fractures.

Hydrothermal fluid alterations are expected to primarily affect migratory fluid elements or LILE (Ottonello et al., 1979; Woodhead et al., 1993). This study confirms this expectation by demonstrating the ΣREE of HFOA was significantly lower than that of CFOA. Furthermore, the Rb, Sr, and Ba contents of both analcime types were strongly

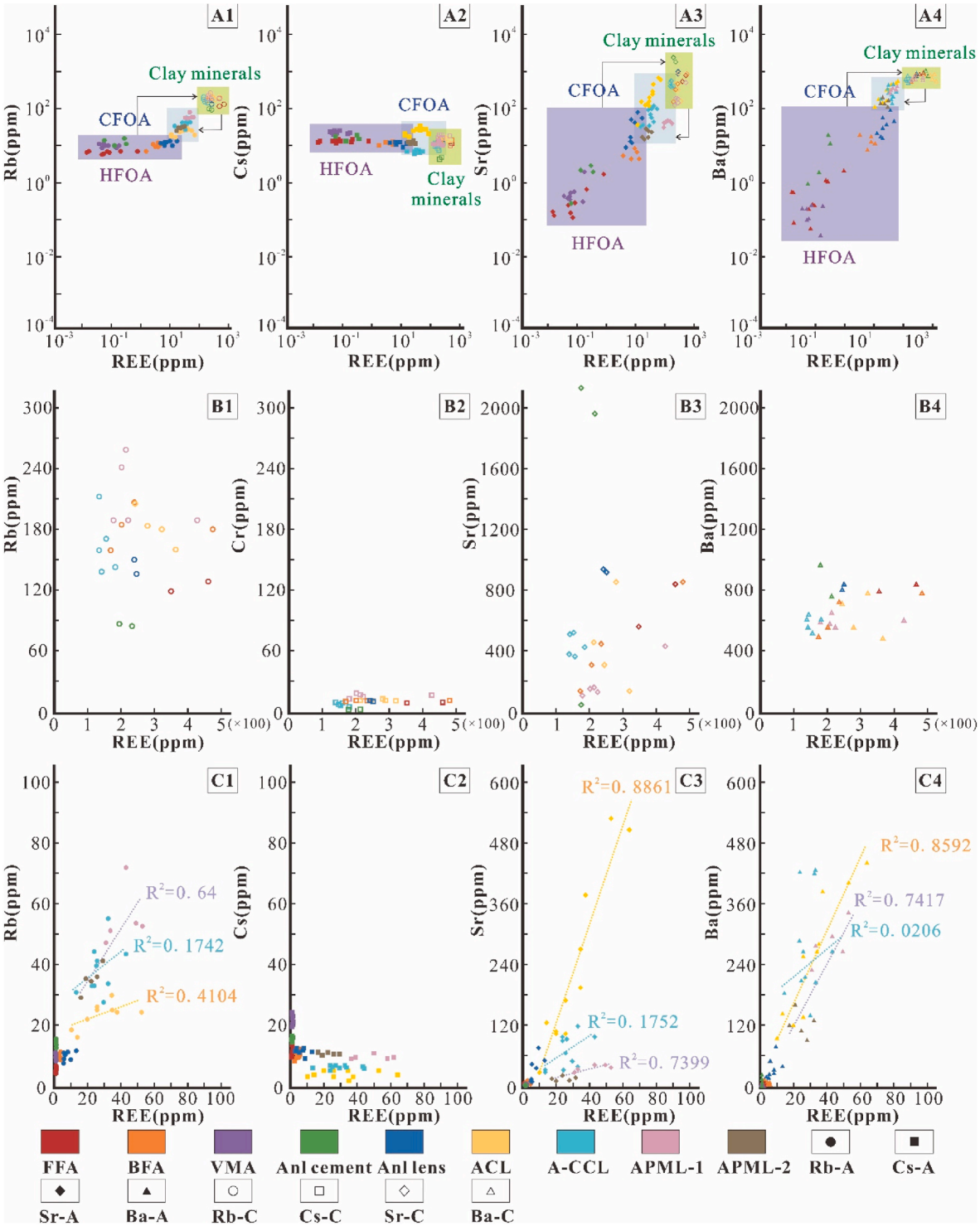

Fig. 11. Enrichment patterns of Rb, Cs, Sr, Ba, and ∑REE. A1-A4. "LILE of analcime and clay minerals (Rb, Cs, Sr, Ba)-∑REE"; B1–B4. "LILE of clay minerals (Rb, Cs, Sr, Ba)-∑REE"; C1–C4. "LILE of analcime (Rb, Cs, Sr, Ba)-∑REE". (X-A, Element-X content of analcime, X = Rb, Cs, Sr, Ba; X–C, Element-X content of clay minerals, X = Rb, Cs, Sr, Ba).

correlated with ∑REE. Specifically, ∑REE decreased with increasing intensity of fluid activities (Fig. 11A1-A4). The Rb contents of HFOA were stable (Fig. 11A1-A2), whereas the Sr and Ba contents were positively correlated with ∑REE (Fig. 11A3-A4). This pattern did not exist in the clay substrate (Fig. 11B1–B4). Although the ∑REEs of CFOA were significantly different from that of HFOA, there were positive correlations with Rb, Sr, and Ba. Calculations of the R^2 led to the conclusion that ACL > A-PML > A-CCL (Fig. 11C1–C4). This reflected that CFOA were affected by fluid reformations, while differences existed within the fluid type and activities intensity.

Accordingly, the degree of positive correlation between Sr and Ba with ∑REE indicates the intensity of fluid activities. The HFOA represented the results of the activities of MHF in the micron-scale fractures at different stages. The three types of CFOA are differentially affected by MHF.

5.3. Mechanism of analcime formation in shales

VMA represents MHF activities near the magma, while FFA represents MHF activities far away from the magma. Analcime cement occurred together with pyrite, filled the spaces between silt-grade clastic particles. Notably, quartz underwent significant erosion (Fig. 12A), and a low-K annular edge was observed in potassium feldspar (Fig. 12B–C). Na ions contributed to the formation of analcime cement, whereas, K ions formed secondary rings around the clastic particles of potassium feldspar. The analcime lens and BFA are mostly concentrated in parapelagic distribution, discontinuous but with laminar characteristics, the 10K/(10K + Na) values of them ranged from 0.02 to 0.11, falling between CFOA and other HOFA types. It possibly as results of MHF activities in shallow bioconcentrated and weakly stratified strata.

Additionally, samples of well GX1 show that HFOA and CFOA appeared as a vertical set, which indicate that the formation process of CFOA was also affected by MHF. The hydrothermal deposition model provides a reasonable explanation for this type of distributional characteristics. When the hydrothermal fluids upwelled into the lake water, thermal repulsions between the crystal particles made it difficult for the particles to form aggregates and precipitate. Instead, the dispersed particles moved far away from the jet outlets and eventually formed a fine-grained sedimentary layer (Trofimovs et al., 2008; Jiao et al., 2018). Analcime laminae is often formed when this layer is modified by Na-rich and high-salinity lacustrine water (Zheng et al., 2006; Li et al., 2016). The combination of different laminae types and minerals might reflect different fluid information (Williams, 1996; Pavelić et al., 2022).

Based on the aforementioned discussion, we proposed that the hydrothermal deposition model was the basis for the formation of analcime laminae in the study area. This mechanism was affected by high-frequency, low intensity tectonic activities throughout the entire depositional period of the second member of the Kongdian Formation. Consequently, various CFOA might reflect climatic information and that on multi-stage hydrothermal activities. VMA and FFA were the results of evolution and crystallization of MHF in micron-scale fractures in different stages, the formation of VMA may earlier than FFA. Fluids entered the silty belts as cement and filled the interparticle spaces to form analcime cement. The formation of analcime lens and BFA was affected by the original rock structure and distributional characteristics of the bioclasts (Fig. 13).

6. Conclusion

Huanghua Depression is located at the intersection of global-scale tectonic zones, has experienced six phases of magmatic activity. Against this background, the hydrothermal fluids from deep mantle-derived magma were the main sources of fluids. During the formation of the shales in the second member of the Kongdian Formation, these fluids were upwelled and exchanged with original sedimentary components of the shale through tensile fractures and ultimately entered the bottom water of the lake, resulting in the formation of analcime as a fluid-tracing mineral.

Analcime can be categorized into six types based on occurrence characteristics (occurring as laminae, lens, fracture filling, bioshell filling, vein marginal crystal and cement). Analcime laminae is further divided into ADML, ACL, and A-CCL. The above six types of analcime is further classified into hydrothermal fluid origin analcime (HFOA: include analcime cement, vein marginal crystal, lens, fracture filling and bioshell filling) and connate fluid origin analcime (CFOA: analcime laminae) based on major elemental indicators (Si/Al and 10K/(10K + Na)). HFOA has lower ∑REE (rare earth element) and strong positive correlation between ∑REE (rare earth element) and LILEs (large ionic lithophilic elements); while CFOA has higher ∑REE and weak positive correlation between ∑REE and LILEs. Analcime with these two origins appeared together in a vertical direction.

The degree of positive correlation between Sr and Ba with ∑REE indicates the intensity of fluid activities, ∑REE decreased with increasing fluid activities intensity. The three types of CFOA are differentially affected by MHF. The HFOA represented the results of the activities of MHF in the micron-scale fractures at different stages, VMA represents MHF activities near the magma, while FFA represents MHF activities far away from the magma. When the fluids entered the silty belt under the influence of ion fractionation and crystallization, analcime serves as cement and filled the interparticle spaces to form analcime cement. The original structure of shale and the distributional characteristics of the bioclasts affected the formation of VMA and BFA.

CRediT authorship contribution statement

Junran Wang: Writing – original draft, Methodology, Investigation,

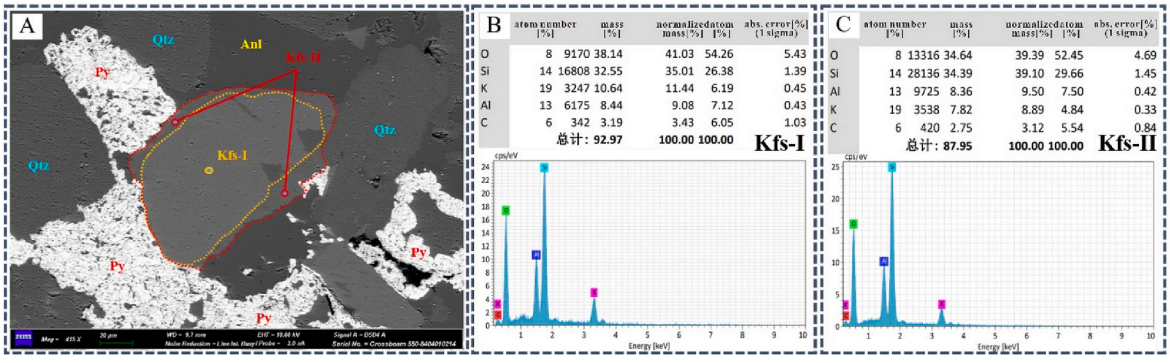

Fig. 12. Distribution of analcime cement and ring margin of potassium feldspar. A. analcime cement distribution characteristics and a low-K annular edge of potassium feldspar; B. Energy spectrum and composition of potassium feldspar particle; C. Energy spectrum and composition of the low-K annular edge of potassium feldspar.

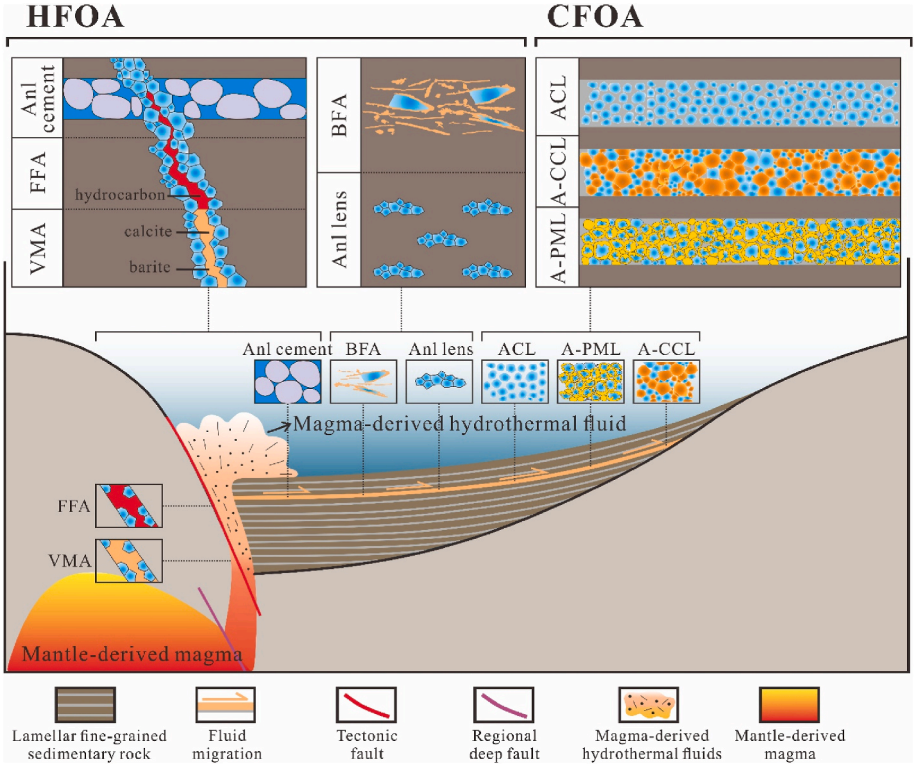

Fig. 13. Formation pattern of analcime in the Cangdong Depression shale layer system.

Data curation, Conceptualization. **Chao Liang:** Writing – review & editing, Visualization, Validation, Supervision, Resources, Project administration, Methodology, Funding acquisition, Conceptualization. **Yingchang Cao:** Supervision. **Shunyao Song:** Resources. **Keyu Liu:** Resources, Supervision. **Shengyu Yang:** Project administration, Resources, Supervision. **Jinqiang Tian:** Resources. **Danish Khan:** Writing – review & editing, Validation, Supervision. **Bixiao Xin:** Resources.

Declaration of competing interest

The authors declare that they have no known competing financial interests or personal relationships that could have appeared to influence the work reported in this paper.

Data availability

Data will be made available on request.

Acknowledgments

The research presented in this paper was supported by the National Natural Science Foundation of China (Nos. 42072164, 41821002), the Shandong Provincial Key Research and Development Program, China (2020ZLYS08), the Fundamental Research Funds for the Central Universities, China (2022CX06001A), Taishan Scholars Program, China (No. TSQN201812030).

References

Barrat, J.A., Boulegue, J., Tiercelin, J.J., et al., 2000. Strontium isotopes and rare-earth element geochemistry of hydrothermal carbonate deposits from Lake Tanganyika, East Africa. Geochimica et Cosmochimica Acta 64 (2), 287–298.

Bennett, S.A., Achterberg, E.P., Connelly, D.P., Statham, P.J., Fones, G.R., German, C.R., 2008. The distribution and stabilisation of dissolved Fe in deep-sea hydrothermal plumes: earth Planet. Sci. Lett., v. 270 (3–4), 157–167.

Boles, J.R., Eichhubl, P., Garven, G., et al., 2004. Evolution of a hydrocarbon migration pathway along basin-bounding faults: evidence from fault cement[J]. AAPG Bull. 88 (7), 947–970.

Boschetti, T., Barbieri, M., Barberio, M.D., Skelton, A., Stockmann, G., Toscani, L., 2022. Geothermometry and water–rock interaction modelling at Hafralækur: possible implications of temperature and CO2 on hydrogeochemical changes previously linked to earthquakes in northern Iceland. Geothermics 105, 102535.

Bradley, W.H., 1928. Zeolite beds in the green river formation. Science 67 (1725), 73–74.

Bradley, W.H., 1929. Occurrence and Origin of Analcime and Meerschaum Beds in the Green River Formation of Utah, Colorado, and Wyoming, 158a. Survey Professional Paper, pp. 1–7.

Bristow, T.F., Milliken, R.E., 2011. Terrestrial perspective on authigenic clay mineral production in ancient Martian lakes. Clay Clay Miner. 59 (4), 339–358.

Cheng, X., Mao, Z., Mao, R., Li, Z., Guan, Q., Chen, X., 2018. Families of reservoired crude oils from the Cangdong sag, Bohai Bay Basin. China: Org. Geochem. 122, 115–125.

Cheng, Y., Wu, Z., Zhang, J., Liu, Y., Dai, Y., 2022. Cenozoic Tectonic Evolution of Offshore Chinese Basins and its Response to Geodynamic Processes of the East Asian Continental Margin. Earth-Sci. Rev., 104140

Chipera, S.J., Goff, F., Goff, C.J., Fittipaldo, M., 2008. Zeolitization of intracaldera sediments and rhyolitic rocks in the 1.25 Ma lake of Valles caldera, New Mexico, USA. J. Volcanol. Geoth. Res. 178 (2), 317–330.

Cole, R.D., Picard, M.D., 1978. Comparative mineralogy of nearshore and offshore lacustrine lithofacies, parachute creek member of the green river formation, piceance creek basin, Colorado, and eastern uinta basin. Utah: Geol. Soc. Am. Bull. 89 (10), 1441.

Columbu, S., 2018. Petrographic and geochemical investigations on the volcanic rocks used in the Punic-Roman archaeological site of Nora (Sardinia, Italy). Environ. Earth Sci. 77 (16), 577.

Coombs, D.S., Whetten, T., 1967. Composition of analcime from sedimentary and burial metamorphic Rocks1: geological society of America bulletin, 78 (2), 269.

Dmitrienko, L.V., Li, S., Cao, X., Suo, Y., Wang, Y., Dai, L., Somerville, I.D., 2016. Large-scale morphotectonics of the ocean-continent transition zone between the Western Pacific Ocean and the East Asian Continent: a link of deep process to the Earth's surface system. Geol. J. 51, 263–285.

Do Campo, M., Del Papa, C., Jiménez-Millán, J., Nieto, F., 2007. Clay mineral assemblages and analcime formation in a Palaeogene fluvial–lacustrine sequence (Maíz Gordo Formation Palaeogen) from northwestern Argentina. Sediment. Geol. 201 (1–2), 56–74.

English, P.M., 2001. Formation of analcime and moganite at Lake Lewis, central Australia: significance of groundwater evolution in diagenesis. Sediment. Geol. 143, 219–244.

Fang, R., Dai, Z., Chen, Z., Shan, J., Jin, K., Zhang, Y., 2020. Characteristics and genesis of analcime in different occurrence states: a case study of the fourth member of Shahejie Formation in Leijia area, western sag, Liaohe depression. Acta Mineral. Sin. 40 (6), 88–100.

Fyfe, W.S., 1997. Deep fluids and volatile recycling: crust to mantle. Tectonophysic. 275 (1–3), 243–251.
Gall, Q., Hyde, R., 1989. Analcime in lake and lake-margin sediments of the carboniferous rocky brook formation, western newfoundland, Canada. Sedimentology 36, 875–887.
Garven, G., 1995. Continental-scale groundwater flow and geologic processes[J]. Annu. Rev. Earth Planet Sci. 23 (1), 89–117.
Giggenbach, W.F., 1988. Geothermal solute equilibria. Derivation of Na-K-Mg-Ca geoindicators: Geochem. Cosmochim. Acta 52 (12), 2749–2765.
Guo, M., Shou, J., Xu, Y., Guo, H., Zou, Z., Han, S., 2016. Distribution and controlling factors of Permian zeolite cements in Zhongguai-Northwest margin of Junggar Basin. Acta Petrolei Sinica 37 (6), 695–705.
Han, G., Wang, L., Xiao, D., Lou, D., Xu, M., Zhao, Y., Pei, Y., Guo, X., Teng, J., Han, Y., 2021. Magmatic hydrothermal fluid genesis of zeolite in the Paleogene Kongdian Formation of zaoyuan oilfield, Bohai Bay Basin. China: Petrol. Explor. Dev. 48 (5), 1101–1112.
Himmler, T., Haley, B.A., Torres, M.E., et al., 2013. Rare earth element geochemistry in cold-seep pore waters of Hydrate Ridge, northeast Pacific Ocean. Geo-marine letters 33, 369–379.
Iijima, A., 2001. Zeolites in petroleum and natural gas reservoirs. Rev. Mineral. Geochem. 45 (1), 347–402.
Iijima, A., Hay, R.L., 1968. Analcime composition in tuffs of the green river formation of Wyoming. Am. Mineral. 53, 184–200.
Jiang, F., Pang, X., Yu, S., Hu, T., Bai, J., Han, G., Li, B., 2015. Charging history of Paleogene deep gas in the Qibei sag. Bohai Bay Basin, China: Mar. Petrol. Geol. 67, 617–634.
Jiao, X., Liu, Y., Yang, W., Zhou, D., Li, H., Nan, Y., Jin, M., 2018. A magmatic-hydrothermal lacustrine exhalite from the Permian Lucaogou Formation, Santanghu Basin, NW China – the volcanogenic origin of fine-grained clastic sedimentary rocks. J. Asian Earth Sci. 156, 11–25.
Keller, W.D., 1952. Analcime in the popo agie member of the chugwater formation. Science 115 (2983), 241–242.
Li, T., 1992. The Statistical Characteristics of the Abundance of Chemical Elements in the Earth's Crust. Geol. Prospect. 28 (10), 1–7.
Li, J., Wang, Y., Liu, C., Dong, D., Gao, Z., 2016. Hydrothermal fluid activity and the quantitative evaluation of its impact on carbonate reservoirs: a case study of the Lower Paleozoic in the west of Dongying sag. Bohai Bay Basin: Petrol. Explor. Dev. 43 (3), 395–403.
Li, Y., Liu, K., Pu, X., Chen, S., Han, W., Zhang, W., Wang, H., Liang, C., Zhao, J., 2020. Lithofacies characteristics and formation environments of mixed FineGrained sedimentary rocks in second member of Kongdian Formation in Cangdong depression, Bohai Bay Basin. Earth Science 45 (10), 3779–3796.
Li, M., Wu, S., Hu, S., Zhu, R., Meng, S., Yang, J., 2021. Lamination texture and its effects on reservoir and geochemical properties of the palaeogene Kongdian Formation in the Cangdong sag, Bohai Bay Basin. China: Minerals 11 (12), 1360.
Liang, J., Wang, H., Bai, Y., Ji, X., Duo, X., 2016. Cenozoic tectonic evolution of the Bohai Bay Basin and its coupling relationship with Pacific Plate subduction. J. Asian Earth Sci. 127, 257–266.
Lin, P., Lin, C., Yao, Y., Wang, B., Li, L., Zhang, X., Zhang, N., 2017. Characteristics and causes of analcime distributed in dolostone of the member 3 of Paleogene Shahejie formationin beitang sag, Bohai Bay Basin. J. Palaeogeogr. 19 (2), 241–256.
Liu, Q., He, L., Chen, L., 2018. Tectono-thermal modeling of Cenozoic multiple rift episodes in the Bohai Bay Basin, eastern China and its geodynamic implications. Int. J. Earth Sci. 107, 53–69.
Liu, Y., Zhou, D., Jiao, X., Feng, Q., Zhou, X., 2019. A preliminary study on the relationship between deep-sourced materials and hydrocarbon generation in lacustrine source rocks: A example from the Permian black rock series in Jimusar sag, Junggar Basin. Journal of Palaeogeography(Chinese Edition) 21 (6), 983–998.
Luo, L., Qi, J., Li, H., Dong, Y., Zhang, S., Zhang, X., Yu, X., Luo, Lingyan, 2017. Geometry and evolution of the Cangdong sag in the Bohai Bay Basin, China: implications for subduction of the Pacific Plate. Sci. Rep. 7 (1), 15393.
Ma, C., Wang, J., Pan, X., Chen, J., Shang, L., Liu, J., 2020. Origin and significance of "sweet spots" of analcites in shale oil reservoirs in permian lucaogou Formation , Jimsar Sag , Junggar basin. Petroleum Geology and Experiment 42 (4), 596–603.
McHenry, L.J., Kodikara, G.R.L., Stanistreet, I.G., Stollhofen, H., Njau, J.K., Schick, K., Toth, N., 2020. Lake conditions and detrital sources of Paleolake Olduvai, Tanzania, reconstructed using X-ray Diffraction analysis of cores. Palaeogeogr. Palaeoclimatol. Palaeoecol. 556, 109855.
Ochoa, M., Arribas, J., Mas, R., et al., 2007. Destruction of a fluvial reservoir by hydrothermal activity (Cameros Basin, Spain). Sedimen. Geol. 202 (1–2), 158–173.
Oliver, J., 1986. Fluids expelled tectonically from orogenic belts: their role in hydrocarbon migration and other geologic phenomena[J]. Geology 14 (2), 99–102.
Ottonello, G., Piccardo, G.B., Ernst, W.G., 1979. Petrogenesis of some Ligurian peridotites—II. Rare earth element chemistry: Geochem. Cosmochim. Acta 43 (8), 1273–1284.
Pavelić, D., Kovačić, M., Tibljaš, D., Galić, I., Marković, F., Pavičić, I., 2022. The transition from a closed to an open lake in the pannonian basin system (Croatia) during the miocene climatic optimum: sedimentological evidence of early miocene regional aridity. Palaeogeogr. Palaeoclimatol. Palaeoecol. 586, 110786.
Prol-Ledesma, R.M., Canet, C., Villanueva-Estrada, R.E., et al., 2010. Morphology of pyrite in particulate matter from shallow submarine hydrothermal vents. American Mineralogist 95 (10), 1500–1507.
Pu, X., Zhou, L., Han, W., Zhou, J., Wang, W., Zhang, W., Chen, S., Shi, Z., Liu, S., 2016. Geologic features of fine-grained facies sedimentation and tight oil exploration: a case from the second Member of Paleogene Kongdian Formation of Cangdong sag, Bohai Bay Basin. Petrol. Explor. Dev. 43 (1), 26–35.
Sanchez-Valle, C., Sinogeikin, S.V., Lethbridge, Z.A.D., Walton, R.I., Smith, C.W., Evans, K.E., Bass, J.D., 2005. Brillouin scattering study on the single-crystal elastic properties of natrolite and analcime zeolites. J. Appl. Phys. 98 (5), 053508.
Savage, D., Walker, C., Arthur, R., Rochelle, C., Oda, C., Takase, H., 2007. Alteration of bentonite by hyperalkaline fluids: a review of the role of secondary minerals. Phys. Chem. Earth 32, 287–297.
Song, B., Han, H., Cui, X., Dong, X., Chen, J., 2015. Petrogenesis analysis of lacustrine analcite dolostone of the Member 4 of Paleogene Shahejie Formation in Liaohe Depression, Bohai Bay Basin. J. Palaeogeo. 17 (1), 33–44.
Su, J., Zhu, W., Wei, J., et al., 2011. Fault growth and linkage: Implications for tectonosedimentary evolution in the Chezhen Basin of Bohai Bay, eastern China. AAPG bulletin 95 (1), 1–26.
Sun, Y., Liu, X., Zhang, Y., Dong, Y., Xu, Y., Shi, G., Lin, Y., Li, A., 2014. Analcime cementation facies and forming mechanism of high-quality secondary clastic rock reservoirs in western China. J. Palaeogeogr. 16 (4), 517–526.
Tao, H., Qiu, Z., Qu, Y., et al., 2022. Geochemistry of Middle Permian lacustrine shales in the Jimusar Sag, Junggar Basin, NW China: Implications for hydrothermal activity and organic matter enrichment. J. Asian Earth Sci. 232, 105267.
Trofimovs, J., Sparks, R.S.J., Talling, P.J., 2008. Anatomy of a submarine pyroclastic flow and associated turbidity current: july 2003 dome collapse, Soufrière Hills volcano, Montserrat, West Indies. Sedimentology 55 (3), 617–634.
Urubek, T., Dolnicek, Z., Kropac, K., 2015. Genesis of syntectonic hydrothermal veins in the igneous rock of teschenite association (Outer Western Carpathians, Czech Republic): growth mechanism and origin of fluids. Geologica Carpathica 65 (6), 419.
Varol, E., 2020. Interpretation of the origin of analcimes with mineralogical, microtextural, and geochemical investigations: a case study from Aktepe region (NE of Kalecik, Ankara, Central Anatolia, Turkey). Arabian J. Geosci. 13 (10), 343.
Wang, G., Li, S., Suo, Y., Zhang, X., Zhang, Z., Wang, D., Guo, L., 2022. Deep-shallow coupling response of the cenozoic Bohai Bay Basin to plate interactions around the Eurasian Plate. Gondwana Res. 102, 180–199.
Wang, J., Liang, C., Cao, Y., Tian, Y., 2022. Occurrence, genesis, and significance of analcime in fine-grained sedimentary rocks. Geofluids 2022, 1–17.
Wang, W., Lin, C., Zheng, M., Lu, S., Wang, M., Zhang, T., 2018. Enrichment patterns and resource prosspects of tight oil and shale oil: A case study of the second member of Kongdian formation in the Cangdong sag, Huanghua depression. J. China Univers. Min. Technol. 47 (2), 332–344.
Williams, W.D., 1996. The largest, highest and lowest lakes of the world: saline lakes. SIL Proceedings 26 (1), 61–79, 1922-2010.
Woodhead, J., Eggins, S., Gamble, J., 1993. High field strength and transition element systematics in island arc and back-arc basin basalts: evidence for multi-phase melt extraction and a depleted mantle wedge. Earth Planet Sci. Lett. 114 (4), 491–504.
Wu, L., Mei, L., Paton, D.A., Liu, Y., Guo, P., Shen, C., Li, M., 2020. Late Cretaceous-Cenozoic intraplate extension and tectonic transitions in eastern China: implications for intraplate geodynamic origin. Mar. Petrol. Geol. 117, 104379.
Xin, B., Zhao, X., Hao, F., Jin, F., Pu, X., Han, W., Xu, Q., Guo, P., Tian, J., 2022. Laminae characteristics of lacustrine shales from the Paleogene Kongdian Formation in the Cangdong Sag, Bohai Bay Basin, China: why do laminated shales have better reservoir physical properties? Int. J. Coal Geol. 260, 104056.
Yang, Q., Qi, J., Chang, D., Li, M., 2009. Tectonopalaeography during the deposition of Paleogene Kongdian Formation in kongnan area, Huanghua depression pf Bohai Bay Basin. J. Palaeogeogr. 11 (3), 306–313.
Yang, Y., Gao, F., Pu, X., 2020. Hydrothermal activities of Paleogene Shahejie Formation in qikou sag and its effects on lacustrine carbonate reservoirs. Journal of China University of Petroleum 44 (2), 20–30.
Yang, Z., Zhou, D., Zhang, S., Guo, Q., Lu, Z., 2018. Mineralogical and Trace-Element Constrains on the Genesis of Zeolite in Lower Cretaceous Lacustrine Rocks from Baiyinchagan Sag, Erlian Basin, China. Earth Science 43 (10), 3733–3748.
Ye, L., 2013. Cenozoic Structure-Stratigraphic Framework and Evolution in the Kongnan Area, Huanghua Depression. A Dissertation Submitted to China University of Geosciences for the Doctor Degree of Engineering.
Zhang, C., Ma, C., Liao, Q., Zhang, J., She, Z., 2011. Implications of subduction and subduction zone migration of the Paleo-Pacific Plate beneath eastern North China, based on distribution, geochronology, and geochemistry of Late Mesozoic volcanic rocks. Int. J. Earth Sci. 100, 1665–1684.
Zhang, S., 2008. "Water Consumption" in the Diagenetic Stage and Its Petroleum Geological Significance. Acta Geologica Sinica 82 (3), 663–668.
Zhang, Y., Chen, S., Meng, Q., Yan, J., Pu, X., 2015. The discovery of analcite in fine-grained sedimentary rocks of the second member of Kongdian Formation in Cangdong sag, Huanghua depression: implications for early digenetic environment. China Petroleum Exploration 20 (4), 37–43.
Zhao, X., Zhou, L., Pu, X., Han, W., Shi, Z., Zhang, W., Shiyue, C., Lu, G., 2018. The sedimentary structure and petroleum geologic significance of the ring belt of the closed lake basin: an integrated interpretation of well and seismic data of the Kong2 Member in Cangdong Sag, Central Bohai Bay Basin. China: Interpretation 6 (2), T283–T298.
Zhao, R., Chen, S., Wang, H., Gan, H., Wang, G., Ma, Q., 2019. Intense faulting and downwarping of nanpu sag in the Bohai Bay Basin, eastern China: response to the cenozoic stagnant pacific slab. Mar. Petrol. Geol. 109, 819–838.
Zhao, X., Pu, X., Jin, F., Han, W., Shi, Z., Cai, A., Wang, A., Guan, Q., Jiang, W., Zhang, W., 2019. Geological characteristics and key exploration technologies of continental shale oil sweet spots: a case study of Member 2 of Kongdian Formation in the Cangdong sag in the Huanghua depression. Bohai Bay Basin: Petroleum Research 4 (2), 97–112.
Zhao, X., Zhou, L., Pu, X., Han, W., Jin, F., Xiao, D., Shi, Z., Deng, Y., Zhang, W., Jiang, W., 2019. Exploration breakthroughs and geological characteristics of

continental shale oil: a case study of the Kongdian Formation in the Cangdong Sag, China. Mar. Petrol. Geol. 102, 544–556.
Zheng, R., Wen, H., Fan, M., Wu, G., Xia, P., 2006. Lithological characteristics of sublancustrine white smoke type exhalative rock of the Xiagou Formation in Jiuxi Basin. Acta Petrol. Sin. 22 (12), 3027–3038.
Zheng, R., Wen, H., Li, Y., Chang, H., 2018. Compositions and texture of lacustrine exhalative rocks from the LowerCretaceous Xiagou Formation in Qingxi sag of Jiuxi Basin, Gansu. J. Palaeogeogra. (Chinese Edition). 20 (1), 1–18.
Zhu, S., Zhu, X., Wang, X., Liu, Z., 2012. Zeolite diagenesis and its control on petroleum reservoir quality of Permian in northwestern margin of Junggar Basin. China: Sci. China Earth Sci. 55 (3), 386–396.
Zhu, S., Cui, H., Jia, Y., Zhu, X., Tong, H., Ma, L., 2020. Occurrence, composition, and origin of analcime in sedimentary rocks of non-marine petroliferous basins in China. Mar. Petrol. Geol. 113, 104164.
Zwicker, J., Smrzka, D., Himmler, T., et al., 2018. Rare earth elements as tracers for microbial activity and early diagenesis: A new perspective from carbonate cements of ancient methane-seep deposits. Chem. Geol. 501, 77–85.